Neurexin and Frizzled signaling intercept axonal-transport at microtubule minus-ends to control synapse formation

Santiago Balseiro-Gómez[1], Yang Yue[2], Lin Shao[1], Selim Çetinkaya[1], Caroline Kuzoian[1], Kristen J Verhey[2], Shaul Yogev[1*]

[1] Department of Neuroscience, Yale School of Medicine, 295 Congress Ave, New Haven, CT 06510

[2] Department of Cell and Developmental Biology, University of Michigan, Ann Arbor, MI 48109

* Corresponding author and lead contact

Contact: shaul.yogev@yale.edu (203) 785-7772

Abstract

Precise synaptic connectivity defines neuronal circuits. Synapse formation is locally determined by transmembrane proteins, yet synaptic material is synthesized remotely and undergoes processive transport in axons. How local synaptogenic signals intercept synaptic cargo in transport to promote its delivery and synapse formation is unknown. We found that control of cargo delivery from microtubule minus-ends mediates pro- and anti-synaptogenic activities of presynaptic Neurexin and Frizzled in *C. elegans*, and identified the atypical kinesin VAB-8/KIF26 as a key molecule in this process. VAB-8/KIF26 levels on synaptic microtubule minus-ends are controlled by Frizzled and Neurexin, its loss mimics *neurexin* mutants or Frizzled hyperactivation, and its overexpression can rescue synapse-loss in these backgrounds. VAB-8/KIF26 protects other minus-end proteins and promotes pausing of retrograde transport to allow delivery into synapses. Consistently, reducing retrograde transport rescues synapse-loss in *vab-8* and *neurexin* mutants. These results uncover an important mechanistic link between synaptogenic signaling and axonal transport.

Introduction

The proper function of complex neuronal circuits hinges on the establishment and maintenance of precisely patterned synaptic connections. Synapse position and numbers are instructed by local pro- and anti-synaptogenic signals from cell adhesion molecules such as Neurexin/Neuroligin and diffusible cues such as Wnts and their Frizzled (Fz) receptors (Sanes and Zipursky, 2020; Südhof, 2018; Yogev and Shen, 2014). In parallel, most synaptic proteins are synthesized in the cell-body and rely on long-range axonal transport to arrive at synapses (Guedes-Dias and Holzbaur, 2019; Maeder et al., 2014; Rizalar et al., 2021). A key question which remains poorly understood is how the activity of synaptogenic signals locally controls the delivery of cargo undergoing transport to generate the appropriate synaptic connectivity pattern.

Presynaptic Neurexins are key synaptse-organizing molecules, with variable context-dependent effects on synapse formation and maturation. Neurexin's extra-cellular domain binds a range of postsynaptic ligands to specify synapse properties (Südhof, 2017). Despite the identification of Neurexin intracellular domain binding proteins, the signaling events downstream of presynaptic neurexin are poorly understood (Biederer and Südhof, 2000; Brouwer et al., 2019; Hata et al., 1996; Owald et al., 2012). Wnts and their Fz receptors are universal signaling molecules with diverse developmental and homeostatic roles. Unlike Neurexin, which largely acts to promote synapse formation or specialization, Fz can either promote or inhibit synapse formation (He Chun-Wei et al.; Koles and Budnik, 2012; Sanes and Zipursky, 2020). Both Fz and presynaptic Neurexin can signal to the synaptic cytoskeleton, although how this promotes or inhibits synapse formation is not well understood (Biederer and Sudhof, 2001; Lüchtenborg et al., 2014; Miech et al., 2008; Muhammad et al., 2015; Sugie et al., 2015).

Synapses rely on long-range microtubule-based transport of synaptic cargo from the cell body (Kreutzberg, 1969). Electron and light-microscopy studies identified "transport packets" containing synaptic vesicle precursors (SVPs) and active zone (AZ) proteins that are delivered by fast axonal transport (Ahmari et al., 2000; Vukoja et al., 2018; Wu et al., 2013; Zhai et al., 2001). Genetic analysis identified the kinesin-3 KIF1A/UNC-104 as the key motor for long-range transport of presynaptic cargo, as cargo is retained in the cell body of kinesin-3 mutants (Hall and Hedgecock, 1991; Okada et al., 1995; Pack-Chung et al., 2007). Intuitively, it is reasonable to expect that all cargo delivery into synapses would occur by local regulation of kinesin-3 at synapses. However, live-imaging studies of *en passant* synapses

clearly show that synaptic cargo is also delivered into presynaptic boutons during retrograde transport from the distal axon towards the cell body, suggesting a role for the retrograde motor dynein (Bharat et al., 2017; Wong et al., 2012). Although several synaptic mechanisms that locally promote capture of dense core vesicles (DCVs) from Kif1A/kinesin-3 at pre and post synaptic sites were identified (Bharat et al., 2017; Stucchi et al., 2018), how cargo capture during retrograde transport is regulated is unknown.

Dynamic microtubule plus-ends are abundant at synapses and were recently shown to promote SVP delivery during anterograde transport by kinesin-3, which runs to the tip of the microtubule and dissociates from the GTP cap (Guedes-Dias et al., 2018; Qu et al., 2019). Studies *in vitro* and in axons have shown that retrograde transport preferentially pauses at microtubule minus-ends (Soundararajan and Bullock, 2014; Tan et al., 2018; Yogev et al., 2016), raising the possibility that these ends might be sites where dynein-driven transport is regulated. However, compared to the large number of proteins identified at microtubule plus-ends, our understanding of microtubule minus-ends in neurons is rudimentary, with few proteins known to reside there (Akhmanova and Steinmetz, 2019; van de Willige et al., 2016).

Here, we found that control of synapse number and positioning by *C. elegans* Neurexin (NRX-1) and the Fz receptor MIG-1 converges on cargo delivery from microtubule minus-ends. We identify the atypical kinesin VAB-8/KIF26 as a microtubule minus-end resident protein that plays a critical role in this process. NRX and Fz signaling locally control the stability of VAB-8/KIF26 on a subset of synaptic microtubules, with degradation of VAB-8/KIF26 by Fz signaling antagonizing the pro-synaptogenic activity of neurexin. Local loss of VAB-8 from synaptic microtubule minus-ends results in impaired distribution of other MT minus-end proteins PTRN-1/CAMSAP and NOCA-1/Ninein, and in excessively processive retrograde transport, which occurs at the expense of cargo delivery and leads to synapse loss. Consistently, reducing dynein activity restores the pattern of presynaptic sites in *vab-8/KIF26* mutants, in *neurexin* mutants, and in a mutant that leads to excessive Fz signaling. These results uncover cargo delivery from microtubule minus-ends as a mechanism for sculping synaptic connectivity by Neurexin and Frizzled signaling.

Results

The Fz receptor MIG-1 acts antagonistically to Neurexin in synapse formation

The *C. elegans* cholinergic motor neuron DA9 resides in the preanal ganglion, from where it extends a dendrite in the ventral cord and an axon that traverses across to the dorsal cord and grows anteriorly, establishing ~25 *en passant* presynaptic sites onto dorsal muscles at stereotypic positions (**Figure 1A**) (White et al., 1986). Expression of the active zone protein Clarinet-1 (CLA-1), homolog of mammalian Piccolo and Bassoon, and the SVP marker RAB-3 allow to visualize DA9 synapses at a single-cell resolution (Chen et al., 2018; Kurshan et al., 2018; Xuan et al., 2017) (**Figure 1B**). In DA9, the sole *C. elegans* Neurexin, *nrx-1,* is required presynaptically for at least two known functions: clustering of RAB-3 vesicles and preventing loss of proximal synaptic boutons (Kurshan et al., 2018) (**Figure 1E**).

We noticed that a mutant isolated in a forward genetic screen for regulators of microtubule minus-ends (see below, Figure 5), *shy20*, also displayed a loss of proximal synapses, highly reminiscent of *nrx-1 (wy778)* mutants (**Figure 1D**), an allele which deletes the α and γ isoforms (For description of alleles, refer to **Table S1**. All alleles used in this study are strong loss of function or null alleles, unless

Figure 1

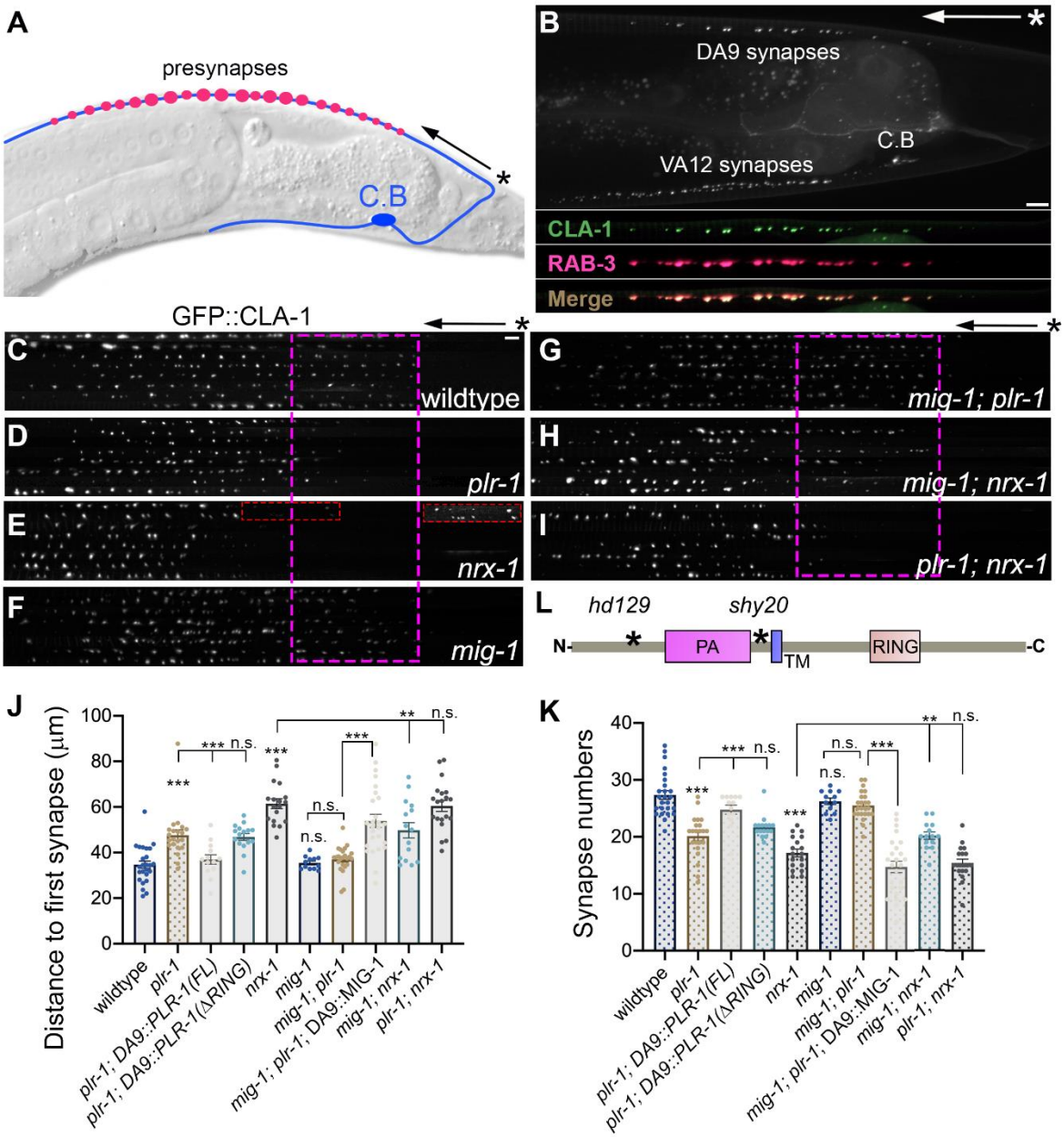

Figure 1: Fz/MIG-1 signaling acts antagonistically to Neurexin in synapse formation.

(A) Schematic of the DA9 motor neuron. ~25 *en passant* presynapses form at stereotypic position along the axon. * and arrow indicate the turn of the commissure and asynaptic domain in all figures. **(B)** wildtype adult expressing the active zone marker GFP::CLA-1 and the synaptic vesicle marker tdTomato::RAB-3 under the Pmig-13 promoter. VA12 synapses on the ventral side are also labelled by the transgene. Bottom panels show a straightened section of the axon beginning at the turn of the commissure (*). C.B, DA9 cell body. Scale bar 5 µm. **(C-I)** *mig-1* partially suppresses *nrx-1* mutants. Confocal images of wildtype (C) and indicated mutant genotypes expressing the synaptic marker GFP::CLA-1. Eight axons per genotype were straightened and aligned from the turn of the commissure (*). Magenta square highlights the missing synapses in *plr-1* and *nrx-1* mutants. Inset in (E) shows fainter proximal CLA-1 puncta in *nrx-1* mutants. These were counted as synapses if their intensity was >5% of the brightest CLA-1 peak. Scale bar 5 µm. **(J, K)** Quantifications of distance to first synapse (J) and synapse numbers (K) in indicated genotypes. ***$p<0.001$; **$p<0.01$; *$p<0.05$ (Mann-Whitney *U* test). **(L)** Domain structure of PLR-1 showing *shy20* and *hd129* allele. PA, protease-associated domain. TM, transmembrane domain. RING, RING finger.

otherwise noted). RAB-3 vesicle clustering around active zones was normal in *shy20* mutants (**Figure S1**), suggesting that *shy20* may be specifically related to Neurexin's function in defining synapse number and position rather than vesicle clustering. Using whole-genome sequencing and genomic rescue experiments, we mapped *shy20* to the transmembrane E3 ubiquitin ligase PLR-1, homolog of mammalian RNF43 and ZNRF3 (**Figure 1L**). *shy20* is a single point mutation that induces a premature stop codon (R188>Opal) before the transmembrane domain, suggesting that it is a strong loss-of-function allele. A second allele, *plr-1(hd129)* showed a similar phenotype to *shy20* (not shown). Using rescue experiments, we determined that PLR-1 functions cell-autonomously in DA9 and that its function requires the RING domain, consistent with a role as a ubiquitin ligase **(Figure 1 J, K)**. Double mutants between *nrx-1* and *plr-1* showed a slight enhancement of the single mutant phenotypes, that was not statistically significant, suggesting that *plr-1* and *nrx-1* function in a common genetic pathway (**Figure 1I, J, K**).

PLR-1 and its mammalian homologs specifically ubiquitinate Frizzled (Fz) receptors to downregulate Fz signaling (Hao et al., 2012; Koo et al., 2012; Moffat et al., 2014). In DA9, the Fz receptor LIN-17 has been shown to mediate anti-synaptogenic functions of its ligand LIN-44, but also to promote synapse-formation independently of LIN-44 (Klassen and Shen, 2007; Kurshan et al., 2018). We therefore speculated that the loss of synapses in *plr-1* mutants was mediated by LIN-17. However, synapse loss in *lin-17; plr-1* double mutants was similar to *plr-1* mutants, indicating that LIN-17 does not function downstream of PLR-1 (**Figure S2**). Consistently, we did not observe changes in the subcellular distribution of LIN-17::YFP in *plr-1* mutants (**Figure S2**). These data are in agreement with a previous study in which LIN-17, unlike other Fz receptors, was not sensitive to PLR-1 overexpression (Moffat et al., 2014). We next examined a second Fz receptor, MIG-1, which does not have a known function in DA9. A MIG-1::GFP transgene expressed in DA9 was enriched in the dendrite but also localized to the axon. In the axon, MIG-1::GFP localized precisely to the region where synapses were lost in *plr-1* mutants (**Figure S3**). This localization is consistent with the presence of source cells secreting Wnt/EGL-20, MIG-1's ligand, in this region, and with the ability of Wnt/EGL-20 to control MIG-1 localization (Mizumoto and Shen, 2013; Pani and Goldstein, 2018). Importantly, mutations in *mig-1* suppressed synapse loss in *plr-1* mutants, strongly suggesting that PLR-1's function is to downregulate MIG-1 signaling to prevent synapse loss (**Figure 1G, J, K**). This suppression was reversed by expression of a MIG-1 transgene in DA9, indicating that MIG-1 signaling functions cell-autonomously (**Figure 1 J, K**).

Since we found that *nrx-1* and *plr-1* function in a common pathway, we next examined *nrx-1; mig-1* double mutants. In these animals, synapse loss was reduced compared to *nrx-1* mutants, although only partially, despite the *mig-1(e1787)* allele being a putative null (**Figure 1H, J, K**). These results indicate that MIG-1 signaling, regulated by PLR-1, acts either downstream or in parallel to Neurexin to antagonize synapse formation. Since NRX-1 also has MIG-1/Fz independent functions, such as RAB-3 vesicle clustering, it likely functions in parallel, rather than upstream, to MIG-1/Fz (**Figure 2I**).

The atypical kinesin VAB-8/KIF26 is required for synapse formation downstream of NRX-1/Neurexin and MIG-1/Fz

We next sought downstream targets of NRX-1 and MIG-1 that could mediate their effect on DA9 synapses. We focused on a second mutant, *shy8,* that displayed a similar phenotype to *plr-1(shy20)* in our microtubule minus-end screen (see below). Examination of GFP::CLA-1 and RFP::RAB-3 in *shy8*

mutants revealed loss of proximal synapses, but no vesicle clustering defects, similar to *plr-1* mutants (**Figure 2B, H, I, Figure S1**). A postsynaptic marker, ACR-12::GFP, was also lost from the same region that showed presynapse loss, confirming the absence of proximal synapses in *shy8* mutants (not shown). *shy8* mapped to *vab*-8, an atypical kinesin homologous to mammalian KIF26A and KIF26B. Kif26A functions in enteric and sensory neurons, where it regulates GDNF-Ret and FAK signaling, respectively. Kif26B functions in cell polarization and migration (Guillabert-Gourgues et al., 2016; Susman et al., 2017; Wang et al., 2018; Zhou et al., 2009) and mutations in human *KIF26B* are associated with progressive microcephaly and spinocerebellar ataxia (Nibbeling et al., 2017; Wojcik et al., 2018). In *C. elegans*, *vab-8* is required for cell migration, axon extension of posteriorly growing neurons and GAP junction localization (Meng et al., 2016; Wightman et al., 1996; Wolf et al., 1998). DA9 grows anteriorly, and we did not detect DA9 axon growth or navigation phenotypes in *vab-8* mutants.

The *shy8* mutation is a 153 bp deletion and frameshift that leads to a premature STOP codon shortly after the motor domain (**Figure 2F**). A CRISPR-induced STOP codon in the same region (*shy72)* was indistinguishable from *shy8* and was used interchangeably. Comparison to previously isolated *vab-8* null alleles (*ev411, gm84, e1017*) or a trans-heterozygote with a genomic deletion encompassing the *vab-8* region (*shy8/arDf1*) revealed similar phenotypic severity (not shown and **Figure S4** for microtubule phenotypes) indicating that *shy8* is a null allele. Expression of VAB-8 in DA9 rescued the *Shy8* phenotype, revealing that it functions cell-autonomously to mediate synapse patterning (**Figure 2G, H**).

To gain further insight into how VAB-8 functions in DA9, we assayed the requirement for its predicted domains in rescue experiments. While full length VAB-8 robustly rescued synapse loss in *vab-8* mutants, constructs lacking the C-terminal coiled-coils or the N-terminal motor domain were inactive, consistent with a function as a motor (**Figure 2G, H**). Furthermore, mutating a conserved residue that is required for kinesin-1 motor domain binding to MTs (R278A) (Woehlke et al., 1997) was sufficient to render VAB-8 inactive (**Figure 2G, H**). These results indicate that microtubule-binding is required for VAB-8 function.

To test whether VAB-8/KIF26 functions downstream of Neurexin and Fz signaling, we conducted double mutant analysis. *vab-8 (shy8)* mutants did not enhance synapse loss of *nrx-1 (wy778)* and *plr-1 (shy20)* mutants, suggesting that the three proteins function in a common genetic pathway (**Figure 2C, G, H**). Unlike the *Plr-1* phenotype, which was suppressed by mutations in *mig-1, mig-1; vab-8* double mutants retained the synapse-loss phenotype of *vab-8* single mutants (**Figure 2G, H**). These observations are consistent with VAB-8 functioning downstream of MIG-1, and therefore also downstream of PLR-1. In agreement with this model, overexpression of VAB-8 in DA9 could ameliorate the phenotype of *plr-1* mutants (**Figure 2G, H**). VAB-8 overexpression also suppressed synapse numbers and mispositioning defects in *nrx-1* mutants (**Figure 2D, E, G, H**). These results indicate that VAB-8 is required for patterning synaptic connectivity downstream of NRX-1 and MIG-1 (**Figure 2I**). A second Wnt receptor, LIN-17 also functions in DA9, where it plays both pro and anti-synaptogenic functions (Klassen and Shen, 2007; Kurshan et al., 2018). *lin-17; vab-8* double mutants mostly resembled *vab-8* mutants (**Figure S2**). Because LIN-17 has both pro and anti synaptogenic activities, we also tested double mutants between *vab-8* and the LIN-17 ligand, LIN-44, which only acts to antagonize synapse formation (Kurshan et al., 2018). *vab-8* mutations suppressed the ectopic synapses that form in *lin-44* mutants, further supporting the notion that VAB-8 is required for synapse formation in the DA9 axon (**Figure S2**).

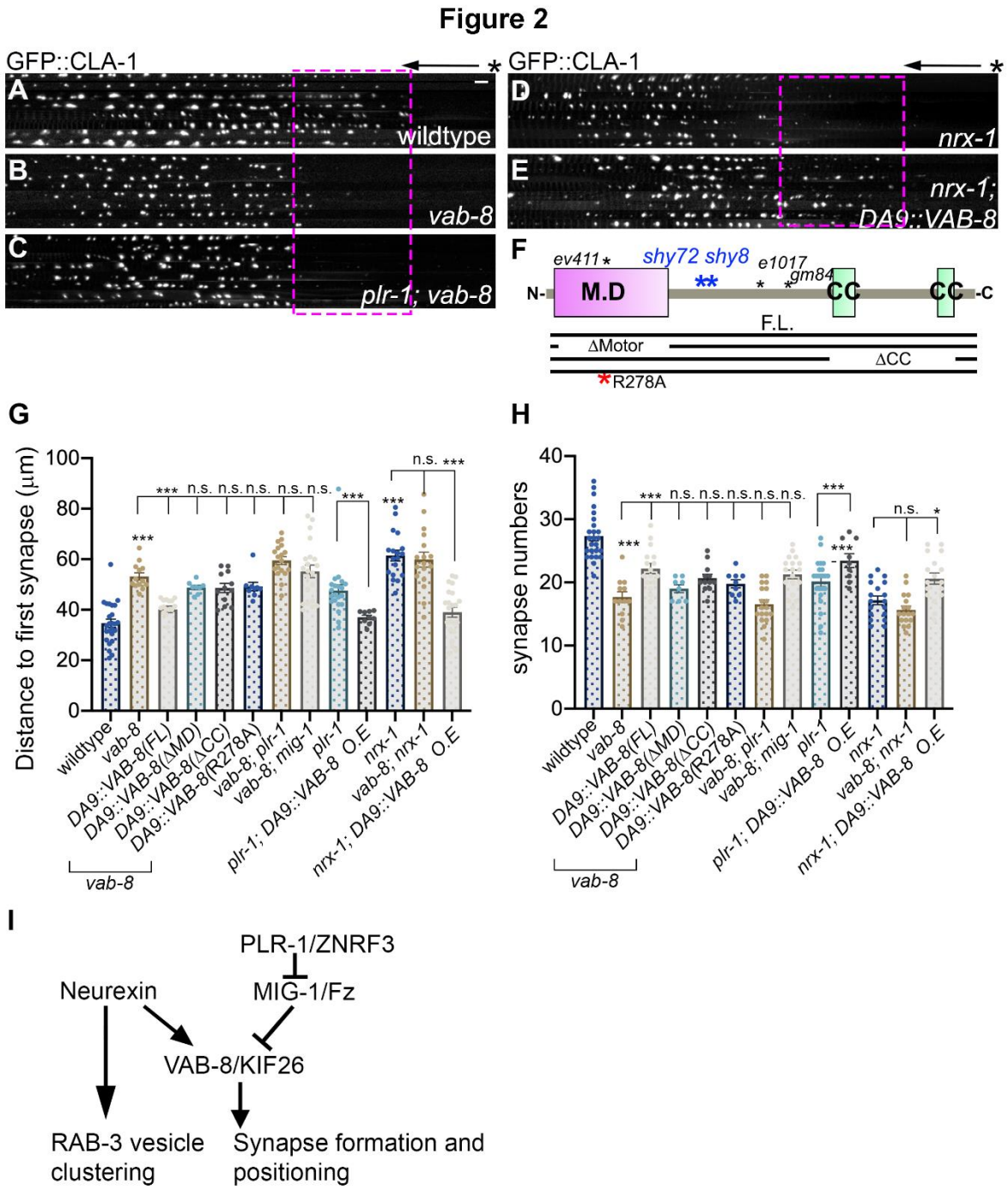

Figure 2: The atypical kinesin VAB-8/KIF26 control synapse formation downstream of NRX-1/Neurexin and MIG-1/Fz

(A-E) Alignments of 8 axons expressing GFP::CLA-1 from confocal images of the following genotypes: wildtype (A), *vab-8* (B), *plr-1;vab-8*(C), *nrx-1* (D), P*mig-13::vab-8* (20ng/μl); *nrx-1* (E). (*) marks turn of the commissure. Scale bar = 5μm. **(F)** Domain structure of VAB-8 showing mutants alleles. Lower bars show rescue constructs. MD, motor domain. CC, coiled-coil domain. **(G-H)** Quantification of the distance from the turn of the commissure to the first synapse (G) and synapse numbers (H). ***p<0.001; **p<0.01; *p<0.05 (Mann-Whitney U test). **(I)** Summary of genetic interactions among *nrx-1, vab-8, plr-1* and *mig-1.* See text for details.

VAB-8 is a microtubule minus-end resident protein in neurons

To gain insight into how VAB-8 controls synapses, we sought to investigate its subcellular localization. Endogenous VAB-8 tagged with 7XspGFP$_{11}$ displayed discrete puncta when visualized with pan-neuronal spGFP$_{1-10}$ (**Figure S4**). Although *vab-8* mRNA is detected in DA9 at the L4 stage, its levels in this neuron were too low for visualizing the endogenous protein with a 7XspGFP$_{11}$ tag (**Figure S4**). A functional VAB-8::GFP transgene expressed in DA9 showed punctate localization throughout the axon (**Figure 3A**), consistent with the distribution we observed for endogenous VAB-8 in other neurons. We noticed that the frequency of VAB-8::GFP puncta is reminiscent of the frequency of microtubule minus-ends in DA9 (Yogev et al., 2016). Microtubules are polar structures, with a fast growing plus-end and a slow-growing minus-end. A large body of research identified many MT-plus-end proteins and their neuronal functions. Conversely, much less is known about regulation of MT minus ends, particularly in neurons (Akhmanova and Steinmetz, 2019; van de Willige et al., 2016). To test whether the VAB-8::GFP puncta we observe in the axon could correspond to MT-minus ends, we co-expressed VAB-8::GFP with RFP::PTRN-1/CAMSAP, which has been extensively validated as a minus-end marker (Feng et al., 2019; Goodwin and Vale, 2010; Jiang et al., 2014; Marcette et al., 2014; Meng et al., 2008; Wang et al., 2015). VAB-8::GFP puncta strongly colocalized with RFP::PTRN-1 puncta (**Figure 3B**), indicating that VAB-8 is minus-end resident protein.

We next asked whether VAB-8 directly binds to MT minus-ends or is recruited there. Interestingly, VAB-8 and KIF26 lack the residues required for ATP hydrolysis. KIF26 shows rigor-like binding to microtubules in co-sedimentation experiments, suggesting that it is likely immotile (Terabayashi et al., 2012; Wolf et al., 1998; Zhou et al., 2009). We used single-molecule TIRF microscopy to image VAB-8::mNeonGreen (mNG) on Taxol-stabilized microtubules in vitro and found that VAB-8::mNG, was mostly immotile. We did not detect directional movement, but note that VAB-8::mNG can diffuse on the microtubule lattice (**Figure 3D**). VAB-8 was not enriched at the minus-end in vitro, suggesting that it is recruited to that location by other proteins in vivo. Consistent with a model in which VAB-8 diffuses on the microtubule to the minus-end, live imaging of VAB-8::GFP in DA9 did not reveal a motile vesicular component (**Figure 3C**). To further test this model, we conducted FRAP experiments: VAB-8::GFP showed an immotile fraction of ~73% and a recovery half-time of ~13 seconds (**Figure 3E**), consistent with a scenario of diffusion on the lattice and capture at the minus-end. We did not observe a significant difference between axon and dendrite, suggesting that the recruitment of VAB-8 to minus ends is not locally regulated.

Finally, we examined whether known non-centrosomal microtubule minus-end proteins recruit VAB-8::GFP to minus-ends. VAB-8::GFP maintained its punctate pattern in *ptrn-1* mutants, suggesting that *ptrn-1* is not required for VAB-8::GFP localization to minus-ends (not shown). In the *C. elegans* germline and epidermis, a Ninein homolog, NOCA-1, localizes to minus-ends of non-centrosomal microtubules and functions redundantly with PTRN-1. A neuronal function for NOCA-1 has not been described (Wang et al., 2015). As *noca-1* mutants are sterile, we examined homozygous progeny of heterozygous mothers, which likely contain maternally contributed *noca-1.* We observed a modest reduction in VAB-8::GFP puncta throughout the axon, with a stronger diffuse component. Interestingly,

Figure 3

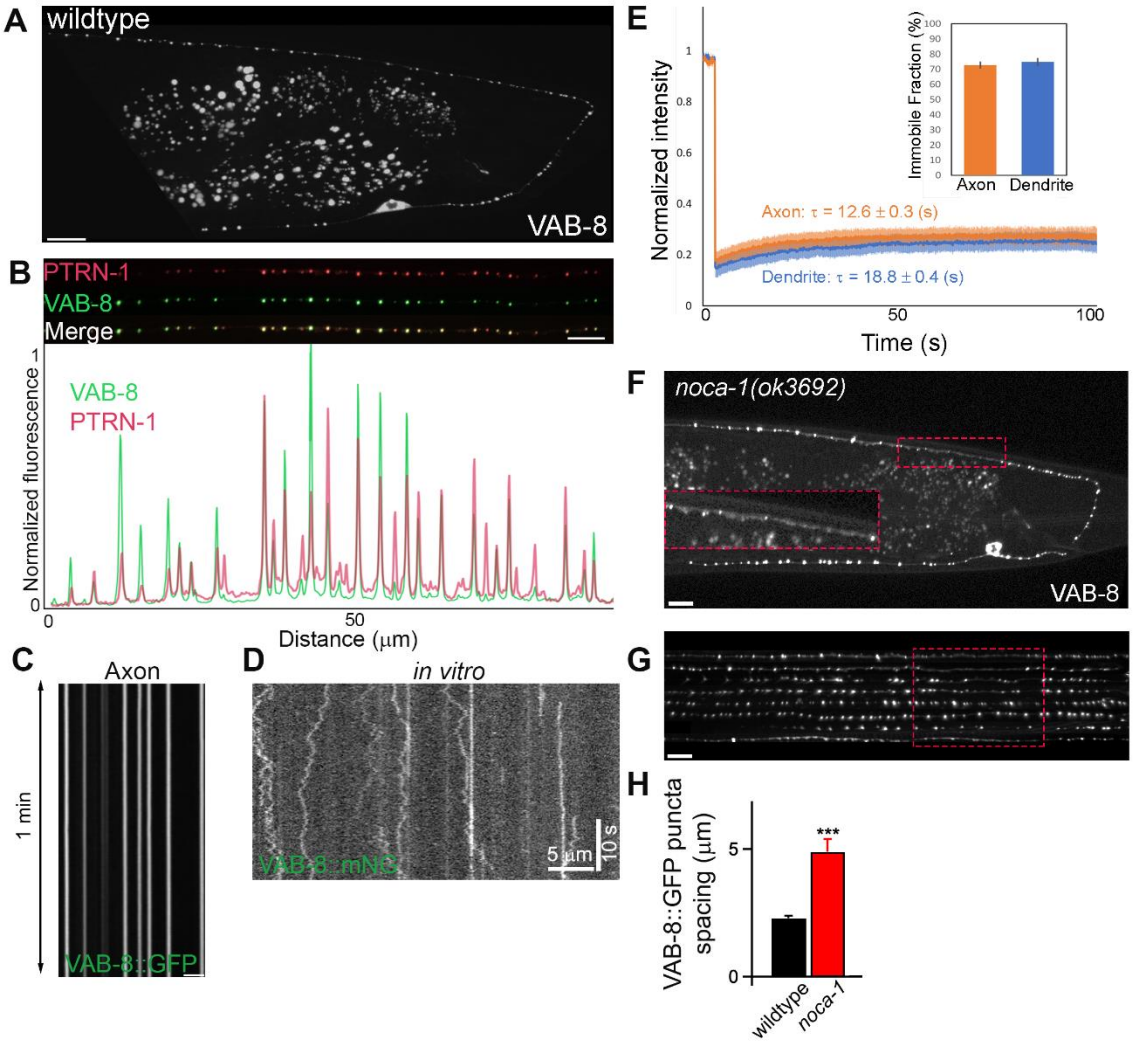

Figure 3: VAB-8 is a microtubule minus-end resident protein in neurons

(A) VAB-8::GFP in wildtype animals shows punctate staining in the axon and dendrite and a microtubule-like pattern in the cell body. Scale bars = 5μm in all panels. **(B)** VAB-8::GFP co-localizes with the microtubule minus-end marker RFP::PTRN-1/CAMSAP. Lower panel shows normalized fluorescence intensity plots. **(C)** Kymograph from a movie of VAB-8::GFP showing no discernible movement. **(D)** Kymograph from a TIRF movie showing VAB-8::mNG on microtubules in vitro. VAB-8 can diffuse on the lattice but does not show directional motility. **(E)** FRAP traces of VAB-8::GFP in the DA9 axon and dendrite reveal that most of the VAB-8 signal is immotile. n=7 per condition. **(F)** *noca-1* is required for the localization of VAB-8. VAB-8::GFP puncta frequency is mildly reduced in *noca-1(ok3692)* mutants derived from heterozygous animals (*noca-1* is required for viability in the embryo), with the strongest effect in proximal synapses. **(G)** Alignment of several axons from the same genotype as (F) shows that the region where VAB-8 loss occurs in *noca-1* mutants is most consistently the proximal synapses. **(H)** Quantification of the average spacing between VAB-8::GFP puncta in wildtype and *noca-1* mutants. n = 20 (wildtype) and 14 (*noca*-1). ***p<0.001 (Mann-Whitney U test).

the most prominent loss of VAB-8::GFP occurred at the proximal synaptic region, where *vab-8* and *plr-1* mutants show loss of synapses (**Figure 3F-H**). An identical distribution of VAB-8::GFP was observed in *ptrn-1; noca-1* double mutants (not shown). Taken together, these data indicate that VAB-8 is recruited to microtubule minus-ends throughout the neuron and is partially stabilized by NOCA-1/Ninein, particularly on the synaptic microtubules in the region controlled by Fz and Neurexin signaling.

NRX-1/Neurexin and MIG-1/Fz control VAB-8/KIF26 accumulation on synaptic microtubule minus-ends

Given that loss of NOCA-1 reduced VAB-8::GFP puncta most drastically in the synaptic domain, we next asked whether local signals in that area control VAB-8 abundance on minus-ends. *plr-1* mutants, in which MIG-1/Fz signaling is increased, showed a drastic elimination of VAB-8 in the proximal synaptic domain (**Figure 4B, G**). Loss of VAB-8 in *plr-1* mutants was more local and severe than in *noca-1* mutants (compare **Figure 4G** with **3H**). Consistent with the synaptic phenotype, this effect could be significantly suppressed by *mig-1* mutants (**Figure 4C, G**), suggesting that the excessive MIG-1/Fz signaling in *plr-1* mutants leads to local VAB-8 degradation. Although we cannot exclude that MIG/Fz interferes with VAB-8 recruitment to minus-ends, we did not observe a significant increase in VAB-8::GFP between puncta. Proteasomal degradation of Kif26B has been previously observed during Kidney development and in migrating cells (Susman et al., 2017; Terabayashi et al., 2012). We next tested whether Neurexin plays a role in VAB-8 stability and found that in *nrx-1* mutants, VAB-8 was also strongly reduced in the synaptic region (**Figure 4D, G**). This reduction was mildly enhanced in *plr-1; nrx-1* double mutants, but the enhancement was not statistically significant. The degradation of VAB-8::GFP in *nrx-1* mutants was partially dependent on MIG-1, since VAB-8::GFP was restored in *mig-1; nrx-1* mutants, although not completely (**Figure 4F, G**) (note that the *mig-1(e1787)* allele used is likely a null since it truncates MIG-1/Fz between its 3rd and 4th transmembrane domains). The effects of *plr-1* and *nrx-1* on VAB-8 stability are in agreement with the ability of overexpressed VAB-8 to suppress the phenotypes of *nrx-1* and *plr-1* mutants (**Figure 2**) and mirror the genetic interaction we observe between *nrx-1, plr-1* and *mig-1* in synapse-patterning. Taken together, these results indicate that regulation of VAB-8 stability on synaptic microtubule minus-ends is an important mechanism for the control of synaptic connectivity by Neurexin and Fz signaling.

VAB-8 is required for stabilizing minus-end proteins on synaptic microtubules

We had originally identified VAB-8 and PLR-1 in a screen for mutants affecting the localization of the microtubule-minus-end marker PTRN-1::YFP in DA9. DA9 has a relatively low abundance of microtubules, similar to cerebellar parallel fibers (Harada et al., 1994), allowing to visualize individual minus-ends with PTRN-1::YFP (Yogev et al., 2016). In wildtype animals, axonal microtubule minus-ends appear with regular periodicity and accumulate an overall uniform level of PTRN-1::YFP (**Figure 5A, D**). In both *vab-8* and *plr-1* mutants, PTRN-1::YFP was reduced at the proximal synaptic area, leading to a local "gap" in the signal (**Figure 5B-F**). This effect was observed in several alleles of *vab-8* and *plr-1*, including nulls (**Figure S5**). Cell specific expression of VAB-8 and PLR-1 in DA9 rescued the phenotype, indicating that both proteins function cell-autonomously (**Figure 5J**). Interestingly, PTRN-1::YFP was not affected in *nrx-1* mutants (not shown, see discussion). Together with VAB-8's localization, these results strongly suggest that VAB-8 functions at MT minus-ends.

Figure 4

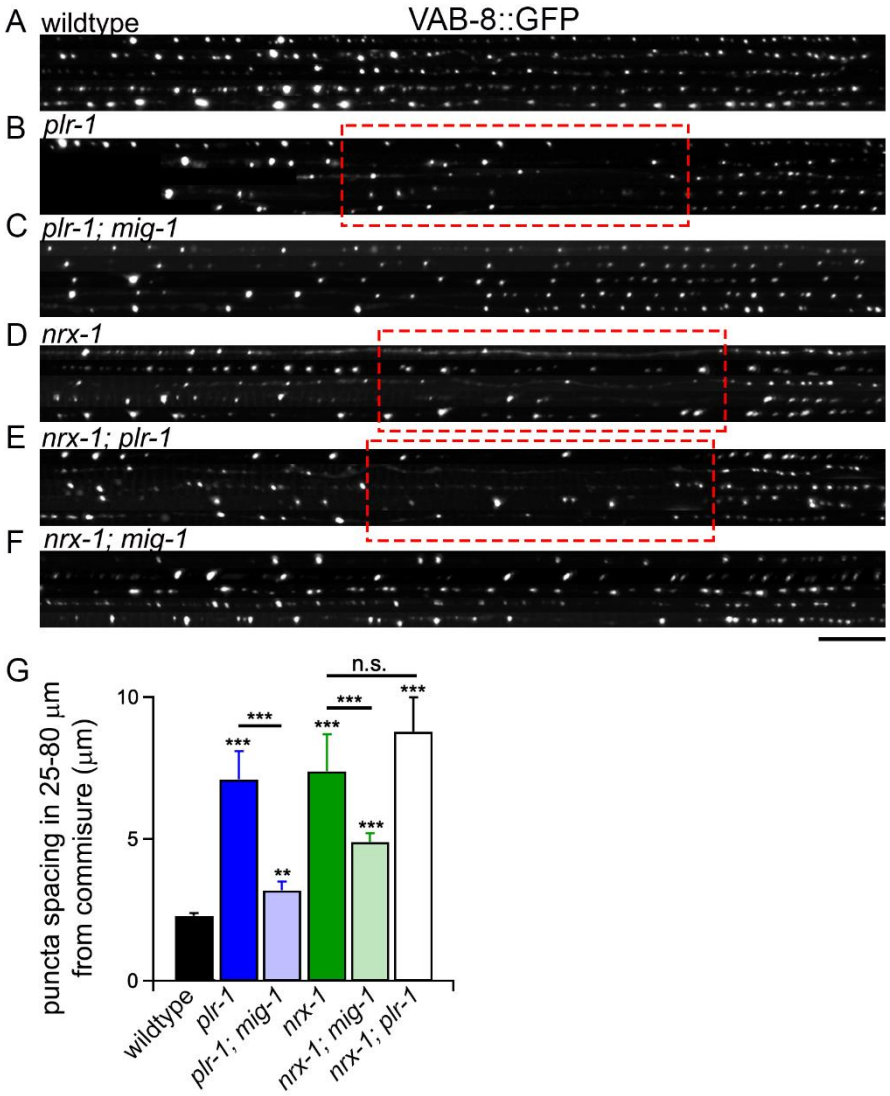

Figure 4: NRX-1/Neurexin and MIG-1/Fz control VAB-8 accumulation on synaptic microtubule minus-ends

(A-F). Confocal images of wildtype (A), *plr-1*(B), *plr-1;mig-1*(C), *nrx-1*(D), *nrx-1;mig-1*(E), *nrx-1;mig-1*(F) axons in DA9 expressing VAB-8::GFP. Five images from each genotype were straightened and aligned to the turn of the commissure (*). Scale bar = 5µm. **(G)** Quantification of spacing between VAB-8::GFP puncta in the region between 25-80 µm from the turn of the commissure. Note that similar to the synaptic phenotype, mutations in *mig-1* partially suppress VAB-8 degradation. n=10-20 per genotype. ***p<0.001; **p<0.01; *p<0.05 (Mann-Whitney U test).

We next asked whether the reduction in PTRN-1::YFP indicates that no polymers start in the affected region, or alternatively reflects a local change in the abundance of minus-end associated proteins. We noted that MTs, labeled with a previously validated GFP::TBA-1/α-tubulin transgene (Yogev et al., 2016), were present in the region where PTRN-1 was reduced (**Figure S6**), suggesting a specific effect on minus-end proteins. To ask whether the dim PTRN-1 puncta in the affected region still localize to minus ends, we tested whether the averaged GFP::TBA-1/α-tubulin intensity around them rises to a peak, as would be expected if they localized to polymer ends. In wildtype animals, RFP::PTRN-1 puncta were associated with a rise in GFP::TBA-1 intensity, whereas locations midway between RFP::PTRN-1 puncta were not (**Figure S7B**). A similar behavior was observed in the affected region of both *plr-1* and *vab-8* mutants (**Figure S7C-F**). These results indicate that VAB-8 is required for the normal accumulation of PTRN-1 on proximal synaptic microtubules, and not for the anchoring of MT minus-ends at this location.

In addition to PTRN-1, we also tested how loss of *vab-8* or *plr-1* affected NOCA-1, a Ninein homolog that localizes to acentrosomal microtubule minus-ends in the hypodermis and germline (Wang et al., 2015). Although PLR-1 is a transmembrane protein and is unlikely to directly affect microtubules, we analyzed *plr-1* mutants because they allow to test the consequences of local loss of VAB-8 from synaptic microtubules. NOCA-1d::GFP showed a punctate distribution similar to PTRN-1::YFP in wildtype animals (**Figure 5G**). In *vab-8* and *plr-1* mutants, NOCA-1d::GFP was specifically reduced, but not completely eliminated, in the proximal synaptic domain, similar to the results obtained with PTRN-1::YFP (**Figure 5G-I**). Similarly to PTRN-1, NOCA-1 was not affected in *nrx-1* mutants (not shown). Together, these results indicate that *vab-8* is locally required for the normal accumulation of other minus-end associated proteins on synaptic microtubules.

To determine the effect of VAB-8 loss on microtubule organization, we imaged animals harboring RFP::PTRN-1 and GFP::TBA-1/α-tubulin in wildtype and mutants. We first analyzed average microtubule length and numbers, using a method that we had previously developed and validated (Yogev et al., 2016, 2017). We observed little differences in the steady-state organization of microtubules between wildtype and *vab-8* or *plr-1* mutants, further suggesting that VAB-8 does not regulate overall microtubule polymer abundance, length or distribution in neurons (**Figure S7**). To determine whether loss of *vab-8* impinges on MT dynamics, we conducted live imaging on GFP::TBA-1/α-tubulin. Visualizing tubulin rather than a plus-end binding protein enables us to measure both polymer growth but shrinkage (**Figure 5K**), which cannot be visualized by end-binding proteins. *vab-8* and *plr-1* mutants displayed a reduction in overall microtubule dynamicity, reflected by lower numbers of both growth and shrinkage events (**Figure 5L**). This phenotype is reminiscent of the reduced microtubule dynamicity in *ptrn-1* mutants (Richardson et al., 2014), in agreement with the local reduction of PTRN-1 in the affected region. We also observed changes in the velocity of growth and shrinkage, yet these effects were milder than the reduced dynamicity and were not consistent across *plr-1* and *vab-8* mutants (**Figure 5M, N**), suggesting that they do not play important roles in the effect of these mutations on synapses. These results identify VAB-8 as a resident protein of microtubule minus ends, which is important to control the levels of other minus-end proteins and polymer dynamics of synaptic microtubules.

Figure 5

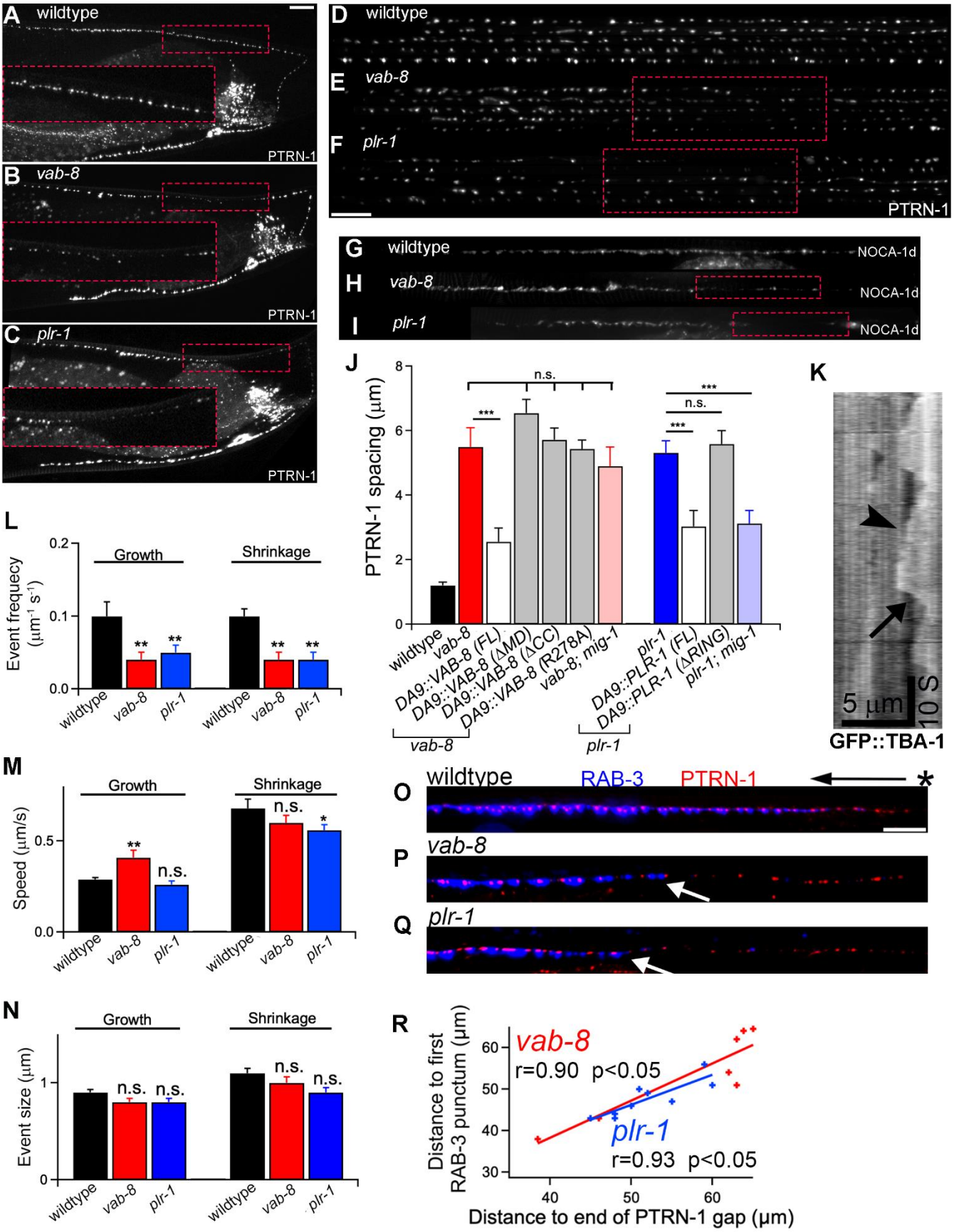
A wildtype
PTRN-1
B vab-8
PTRN-1
C plr-1
PTRN-1
D wildtype
E vab-8
F plr-1
PTRN-1
G wildtype
NOCA-1d
H vab-8
NOCA-1d
I plr-1
NOCA-1d
J
PTRN-1 spacing (µm)
n.s.
***
wildtype
vab-8
DA9::VAB-8 (FL)
DA9::VAB-8 (ΔMD)
DA9::VAB-8 (ΔCC)
DA9::VAB-8 (R278A)
vab-8; mig-1
plr-1
DA9::PLR-1 (FL)
DA9::PLR-1 (ΔRING)
plr-1; mig-1
vab-8
plr-1
K
5 µm
10 s
GFP::TBA-1
L
Growth
Shrinkage
Event frequecy (µm⁻¹ s⁻¹)
wildtype
vab-8
plr-1
M
Speed (µm/s)
n.s.
O wildtype
RAB-3
PTRN-1
P vab-8
Q plr-1
N
Event size (µm)
R
vab-8
r=0.90 p<0.05
plr-1
r=0.93 p<0.05
Distance to first RAB-3 punctum (µm)
Distance to end of PTRN-1 gap (µm)

Figure 5. **VAB-8 is required for stabilizing minus-end proteins on synaptic microtubules and cargo accumulates distally to the region affected in *vab-8* mutants**

(A-C) Distribution of the microtubule minus-end marker PTRN-1::YFP in wildtype (A), *vab-8* (B), and *plr-1* mutants (C). Insets show the loss of PTRN-1 from the proximal synaptic region in the mutants. Scale bar 5μm in all panels. **(D-F)** Straightened axons from several animals per genotype highlight the stereotypic location where PTRN-1 is lost in the mutants. **(G-I)** A second microtubule minus-end associated protein, NOCA-1d, is specifically reduced in the proximal synaptic domain of *vab-8* (H) and *plr-1* mutants (I) compared to wildtype (G). **(J)** Quantification of PTRN-1::YFP puncta spacing in the indicated genotypes. N = 15-25 per genotype. ***p<0.001 (Mann-Whitney U test). **(K-N)** Microtubule dynamics in the DA9 axon were quantified on kymographs from movies of the microtubule marker GFP::TBA-1/α-tubulin (K). Arrowhead points to polymer growth and arrow points to shrinkage. Overall polymer dynamicity (number of growth and shrinkage events) is reduced in both *vab-8* and *plr-1* mutants (L). The speed of microtubule growth and shrinkage (M) in the mutants shows minor differences from wildtype whereas the size of these events (N) is similar in all genotypes. n = 20-30 per genotype. **p<0.01 (Mann-Whitney U test). **(O-Q)** Co-expression of PTRN-1::YFP and and tdTomato::RAB-3 shows at least one microtubule minus-end in each synapse in wildtype (O). In *vab-8* (P) and *plr-1* (Q) mutants, synaptic cargo accumulates distal to the region showing defects in PTRN-1. **(R)** Correlation between PTRN-1::YFP gaps and distance to first synapse/tdTomato::RAB-3 in *vab-8* (red) and *plr-1* (blue) mutants. n = 12 (*vab-8*) and 20 (*plr-1*). r Pearson value and statistical significance (Student t test) are showed.

VAB-8 function at microtubule minus ends is related to its synaptic function

To understand how VAB-8 function at microtubule minus ends might be related to its role in controlling synapse numbers and location, we first tested whether both functions require the same protein domains. Cell-specific rescue experiments showed that both VAB-8 and PLR-1 act to maintain the normal distribution of PTRN-1 through the same domains that are required for synapse formation. (**Figure 5J**). Furthermore, *vab-8* and *plr-1* mutants showed the same genetic interactions with each other and with *mig-1* that were observed for the synaptic phenotype (**Figure 5J**). These results suggest that VAB-8 function at microtubule minus ends is related to its synaptic function.

One possibility is that loss of synapses is the primary defect, which then impairs the recruitment of PTRN-1 to minus-ends. To test this, we examined mutations in kinesin-3/KIF1A *unc-104 (e1265)*, in which DA9 synapses are largely eliminated (Hall and Hedgecock, 1991; Ou et al., 2010). *unc-104(e1265)* mutants did not show a significant reduction in the recruitment of PTRN-1::YFP to discrete puncta, arguing that synapse loss is not the reason for the loss of PTRN-1 from minus-ends in *vab-8* mutants (**Figure S5**). We next asked whether reduced PTRN-1 or reduced microtubule dynamicity could underlie the synaptic phenotype. However, DA9 synapses were largely unaffected in *ptrn-1* mutants or in a β-tubulin/ *tbb-2 (qt1)* mutant that strongly suppresses microtubule dynamics in DA9 (Yogev et al., 2017) (**Figure S5**). We conclude that loss of synapses does not impair PTRN-1 recruitment and that reduced PTRN-1 and microtubule dynamicity do not cause the synaptic phenotype.

VAB-8 promotes cargo pausing during axonal transport

We next turned to the regulation of axonal transport as a possible link between VAB-8 function at microtubule minus-ends and synapses. Local regulation of cargo delivery from minus-ends into synapses is plausible because the frequency of minus-ends is higher than that of synapses, such that in wildtype DA9 every synapse is associated with at least one microtubule minus-end (**Figure 5O**). We

previously showed that during SVP transport, most kinesin-3/UNC-104 and dynein dependent runs terminate at microtubule ends (Yogev et al., 2016), raising the possibility that UNC-104 could be regulated at the plus-end and dynein at the minus-end. We distinguished three possible scenarios: first, If VAB-8 at minus-ends is indirectly affecting synapses, we would not expect the PTRN-1 gap to precisely correlate with the missing synapses in individual animals. Alternatively, if VAB-8 functions to regulate cargo delivery during anterograde transport, synaptic material should accumulate proximal to the gap. Lastly, if VAB-8 mediates cargo delivery during retrograde transport, synapses should form distal to the gap. Co-labelling of RAB-3 and PTRN-1 showed a striking correlation between these markers in individual *vab-8* and *plr-1* animals (**Figure 5P-R**). Furthermore, synapses invariably formed distal to the gap, consistent with a failure in cargo delivery during retrograde transport (**Figure 5P-R**).

To test this model directly, we conducted live imaging of SVP transport. We photobleached the region affected by *vab-8* mutants and imaged the SVP marker GFP::RAB-3 at 10 Hz (**Figure 6A**). We compared wildtype to *vab-8* and *plr-1* mutants, in which VAB-8 is specifically lost from synapses. Kymograph analysis of the movies showed minor changes in instantaneous velocity of cargo movement in *plr-1* mutants, but not *vab-8* mutants (**Figure 6B**). These results agree with the observation that VAB-8 is not detected as moving vesicular puncta and suggest that VAB-8 does not directly affect the ability of motors to transport cargo. We also did not detect significant changes to the overall ratio of anterograde to retrograde transport, suggesting that VAB-8 does not regulate overall cargo flux (**Figure 6C**).

We next examined cargo pausing during transport. Excessive pausing by kinesin-3/UNC-104 is associated with premature synapse formation in *C. elegans*, and pausing facilitates synaptic cargo retention in cultured hippocampal neurons (Guedes-Dias et al., 2018; Wu et al., 2013). In both *plr-1* and *vab-8* mutants, the number of pauses during transport was significantly decreased (**Figure 6E**). Furthermore, pauses were also shorter in either mutant compared to wildtype (**Figure 6F**). These results indicate that VAB-8 functions to promote pausing during transport, potentially to facilitate cargo delivery. Consistent with VAB-8 localization to microtubule minus ends, pause frequency was mostly affected during dynein-driven retrograde transport (**Figure 6G**). In addition, we also observed that cargo run length was increased in both mutants (**Figure 6D**). Run-length increase is consistent with the reduction in pausing frequency and duration, which is expected to increase run length when pauses are shorter than our temporal resolution of 100 ms. These results identify VAB-8 as a regulator of synaptic cargo transport, with its strongest effect being on pausing during retrograde transport.

Synapse loss in *vab-8* and *nrx-1* mutants is due to excessive dynein-driven retrograde transport

To test whether reduced pausing at microtubule ends is responsible for synaptic defects in *vab-8* mutants, we asked whether compromising the processivity of axonal transport would rescue the synaptic phenotypes in *vab-8* mutants. Although the specific localization of VAB-8 to minus-ends and the more pronounced retrograde transport defects point to dynein as the relevant motor protein, our live-imaging data revealed reduced pause duration and increased run length also in the anterograde direction, probing us to also test the involvement of kinesin-3/UNC-104. To compromise transport in the anterograde direction we chose weak alleles of kinesin-3/UNC-104 and its activator ARL-8 (*wy711* and *tm2388,* respectively) (Niwa et al., 2016; Wu et al., 2013) and to compromise retrograde transport we chose a weak allele of dynein heavy chain *dhc-1 (js319)* and its regulator NDEL1 *nud-2 (ok949)* (Koushika et al., 2004; Ou et al., 2010). We confirmed previous observations, that these single mutants do not

Figure 6

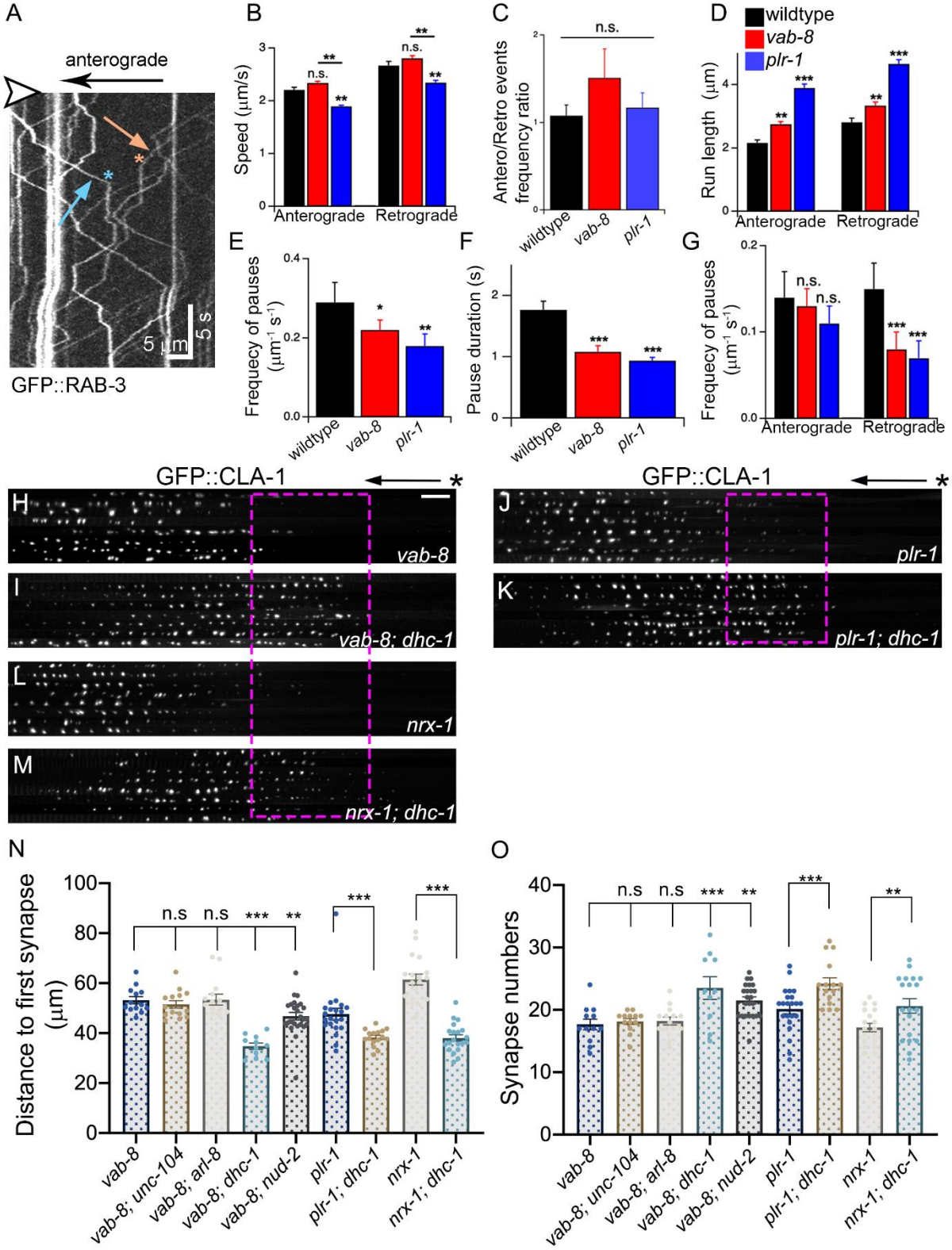
A
anterograde
5 μm
5 s
GFP::RAB-3
B
Speed (μm/s)
n.s.
**
Anterograde
Retrograde
C
Antero/Retro events frequency ratio
n.s.
wildtype
vab-8
plr-1
D
wildtype
vab-8
plr-1
Run length (μm)
Anterograde
Retrograde
E
Frequecy of pauses (μm⁻¹ s⁻¹)
F
Pause duration (s)
G
Frequecy of pauses (μm⁻¹ s⁻¹)
GFP::CLA-1
H
vab-8
I
vab-8; dhc-1
L
nrx-1
M
nrx-1; dhc-1
J
plr-1
K
plr-1; dhc-1
N
Distance to first synapse (μm)
n.s
***
vab-8
vab-8; unc-104
vab-8; arl-8
vab-8; dhc-1
vab-8; nud-2
plr-1
plr-1; dhc-1
nrx-1
nrx-1; dhc-1
O
Synapse numbers

Figure 6: Synapse loss in *vab-8* and *nrx-1* mutants is due to excessive dynein-driven retrograde transport

(**A)** Example kymograph from a GFP::RAB-3 movie. Arrowhead indicates photobleaching, arrows and asterisks show runs terminating in pauses. **(B-G)** Quantification of SVP (GFP::RAB-3) transport in the DA9 axons from wildtype, *vab-8* and *plr-1* animals showing overall more processive transport in the mutants, particularly in the retrograde direction. Vesicle speed (B) or the ratio of anterograde to retrograde events (C) are similar in wildtype and mutants. Cargo run length (D) is increased in both mutants, whereas pause frequency is reduced (E) and pause duration increases (F). Pause frequency is specifically affected in the retrograde direction (G). n = 20-30 animals per genotype. ***p<0.001; **p<0.01; *p<0.05 (Mann-Whitney *U* test). **(H-M)** Reducing dynein function rescues synaptic defects in *vab-8, plr-1* and *nrx-1* mutants. Images show 8 axons expressing GFP::CLA-1 aligned to the turn of the commissure. Genotypes: *nrx-1* (H), *nrx-1; dhc-I* (I); *vab-8* (J), *vab-8; dhc-I* (K), *plr-1* (L), *plr-1; dhc-I* (M). Scale bar 5μm. **(N-O)** Quantification of distance to first synapse/CLA-1 punctum (N) and synapse numbers (O) in the indicated genotypes. ***p<0.001; **p<0.01; (Mann-Whitney *U* test).

display overt synaptic defects, with the exception of *arl-8 (tm2388)* which shows a mild posterior shift in synapse location (not shown) (Ou et al., 2010; Wu et al., 2013).

Double mutants between *vab-8* and *unc-104 (wy711)* or *arl-8 tm2388)* displayed a similar phenotype to *vab-8* single mutants (**Figure 6N, O**), suggesting that mis-regulated anterograde transport does not play causal roles in the steady-state *Vab-8* phenotype. In striking contrast, reducing retrograde transport in *vab-8* mutants, either with *nud-2 (ok949)* or more drastically with *dhc-1 (js319)*, significantly rescued synapse numbers and positioning (**Figure 6H, I, N, O**). These results argue that VAB-8 regulates synapse formation and position by antagonizing dynein-driven transport.

Since we observed that VAB-8 functions downstream to PLR-1 and Neurexin, we extended the analysis to ask whether excessive retrograde transport also underlies synapse loss in these mutants. Previous live-imaging of cargo transport in *nrx-1* mutants indeed revealed an increase in processivity that is highly reminiscent of our observations in *vab-8* and *plr-1* mutants (Kurshan et al., 2018). *dhc-1(js319)* robustly suppressed the synaptic phenotypes of *plr-1* (**Figure 6J, K, N, O**). *dhc-1(js319)* also strongly suppressed the synapse-positioning defects of *nrx-1* mutants and led to an increase in synapse numbers (**Figure 6L-O**). Taken together, our results identify the regulation of retrograde transport at microtubule minus-ends by VAB-8 as an important mechanism through which Neurexin and Frizzled signaling sculpt synaptic connectivity.

Discussion

How the synaptogenic activity of cell-surface molecules promotes the local delivery of synaptic cargo undergoing long-range transport is poorly understood. Here we describe a role for the immotile kinesin VAB-8/KIF26 in linking Neurexin and Frizzled signaling to the delivery of synaptic cargo undergoing retrograde transport. We find that the levels of VAB-8 at microtubule minus-ends are locally regulated by MIG-1/Fz and Neurexin signaling in a subset of presynaptic sites. In *vab-8* mutants, or when VAB-8 levels are locally reduced in this region in *plr-1* and *nrx-1* mutants, those specific synapses are lost. Conversely, VAB-8 overexpression can ameliorate synapse-loss in *plr-1* and *nrx-1* mutants, suggesting that it is an important mediator of PLR-1's and Neurexin's presynaptic function. In *vab-8* mutants, *nrx-1* mutants (Kurshan et al., 2018) and *plr-1* mutants, retrograde axonal transport becomes overly processive. Importantly, synapse-loss in these mutants can be rescued by compromising retrograde transport. Together, these results strongly support a model in which the pro- and anti-synaptogenic activities of Neurexin and Fz converge on VAB-8/KIF26 to regulate the delivery of synaptic cargo undergoing retrograde transport from microtubule minus-ends. This model is further supported by the localization of both paused dynein (Yogev et al., 2016) and VAB-8/KIF26 to microtubule minus-ends, and by the specific formation of synapses distally to the affected region in *vab-8* mutants.

Synaptogenic activity promotes the local delivery of cargo undergoing transport

Synapse formation entails the recruitment of actin, scaffolding and active zone molecules, and vesicle precursors (Rizalar et al., 2021; Südhof, 2018). Although binding partners for Neurexin's intracellular domain have been identified, how Neurexin functionally promotes presynapse formation is not yet understood. Neurexin's intracellular domain binds the scaffolding proteins CASK and MINT, and Neurexin clustering can promote synaptic vesicle recruitment (Biederer and Südhof, 2000; Biederer and Sudhof, 2001; Dean et al., 2003; Hata et al., 1996; Mukherjee et al., 2008). In *Drosophila*, Neurexin binds the active zone molecule SYD-1 and the actin binding protein Spinophilin (Muhammad et al., 2015; Owald et al., 2012). Our results identify the regulation of cargo delivery during axonal transport as an important facet of Neurexin's synaptogenic activity: synapse loss in *nrx-1* mutants is rescued by VAB-8 overexpression or by reducing retrograde transport. Wnt/Fz signaling is also well known to regulate synaptogenesis, although unlike Neurexin, it often plays inhibitory roles (He Chun-Wei et al.). Synaptic Fz signaling in *Drosophila* is important for proper cytoskeletal organization, but exactly how those relate to transport is unclear (Lüchtenborg et al., 2014; Miech et al., 2008; Sugie et al., 2015). Our data show that degradation of VAB-8/KIF26 is a mechanism for antagonizing synapse formation by MIG-1/Fz and reveal that VAB-8 is required for ectopic synapse formation in *lin-44/Wnt* mutants. However, they do not address how Fz/LIN-17 positively regulates synapse-formation. Importantly, linking VAB-8 to synaptic cargo delivery from microtubule ends provides a plausible mechanism for how the control of cytoskeletal proteins by Wnt/Fz signaling regulates synaptogenesis.

Transport pausing at microtubule minus-ends facilitates cargo capture by synapses

Most synaptic proteins are synthesized in the cell body and rely on long-range microtubule-dependent transport to reach synapses (Ahmari et al., 2000; Kreutzberg, 1969). Local cargo delivery, the last step in transport prior to retention/capture at a synaptic site, is still poorly understood. Live imaging of DCVs revealed that their delivery occurs during both anterograde and retrograde transport and is promoted by synaptic activity (Bharat et al., 2017; Cavolo et al., 2016; Wong et al., 2012). However, how

delivery is regulated by synaptogenic signals is still elusive. We found that VAB-8/KIF26 is locally controlled by Neurexin and Frizzled signaling to promote cargo delivery to a specific subset of synapses. Furthermore, in the absence of *vab-8* these synapses are missing, highlighting the importance of local regulation of cargo delivery as a mechanism to control synapse formation. Interestingly, distal synaptic boutons in DA9 were not affected by *vab-8, nrx-1* or *plr-1* mutations, raising the possibility that delivery during anterograde transport plays a more prominent role in those distal synapses.

DCV capture/retention is promoted by interactions of kinesin-3/KIF1A with the scaffolding molecules liprin-α and TANC2 at dendritic spines, and DCV dissociation from kinesin-3 is enhanced by JNK-dependent phosphorylation of Synaptotagmin-4 at presynaptic sites (Bharat et al., 2017; Stucchi et al., 2018). Because cargo needs to bypass many *en passant* synapses to ensure uniform distribution among all sites, these – and potentially other – synaptic capture mechanisms operate at a low probability (~1% for SVPs in cultured hippocampal neurons (Guedes-Dias et al., 2018)). Hence, pausing during transport is likely important to allow synaptic capture mechanisms to engage with motor-cargo complexes.

Kinesin-3 and dynein pause on microtubule plus and minus-ends, respectively (Cai et al., 2009; Soundararajan and Bullock, 2014; Tan et al., 2018; Yogev et al., 2016). kinesin-3 shows lower affinity for the GTP cap, and therefore an association between dynamic plus-ends and synapses was proposed to promote cargo delivery by kinesin-3 (Guedes-Dias et al., 2018). This suggests that the increased anterograde processivity of SVPs that we observe in the absence of VAB-8 may stem from the reduced plus-end dynamics in the mutants. Alternatively, it could be a by-product of losing synaptic capture mechanisms, as proposed in the case of *nrx-1* mutants (Kurshan et al., 2018). Importantly, suppression of *Vab-8* phenotypes by *dhc-1* and *nud-2* but not *unc-104 and arl-8* allows us to distinguish which dynamic transport parameters are causal for the steady-state synaptic phenotype. The conclusion that overly processive retrograde transport drives synapse loss is also supported by the association between minus ends and synapses and the accumulation of cargo distally, rather than proximally, to the affected region in the mutants. We propose that reduced pausing, which is mostly observed in the retrograde direction, is the most relevant parameter because of the inefficiency of synaptic capture mechanisms, which may be unable to engage with moving cargo.

VAB-8/KIF26 function at microtubule minus ends

How does VAB-8 regulate retrograde transport and the accumulation of minus-end proteins? Our TIRF imaging suggests that VAB-8 does not directly identify the structure of the minus-end but is recruited to these locations, at least partially by NOCA-1. Since in *vab-8* mutants the reduction in PTRN-1 and NOCA-1 – both of which directly bind minus ends (Goodwin and Vale, 2010; Meng et al., 2008; Wang et al., 2015) – is restricted to the synaptic region and is not accompanied by a redistribution of these proteins to other parts of the neuron, we favor a model where synaptic VAB-8 protects other minus-end proteins from degradation. Consistently, proteasomal degradation controls Kif26b levels during kidney development and in cultured mesenchymal cells exposed to Wnt 5A-Ror signaling (Susman et al., 2017; Terabayashi et al., 2012). Interestingly, in the absence of VAB-8 and MIG-1, degradation of PTRN-1 was still observed at proximal synapses, although it was reduced. Furthermore, while VAB-8 was strongly reduced in *nrx-1* mutants, PTRN-1 and NOCA-1 were not. Together, these observations suggest that an additional signal regulates the composition of minus-end protein complexes in the synaptic region, possibly downstream of Neurexin. This scenario is also consistent with

the observation that *mig-1* and *dhc-1* mutants, as well as VAB-8 over-expression, rescue *nrx-1* mutations to a lesser extent than that observed for *plr-1.* Precisely how VAB-8 promotes pauses of dynein remains to be elucidated. Kif26a was proposed to anchor and regulate kinase pathways on the microtubule lattice (Wang et al., 2018; Zhou et al., 2009), raising the possibility that VAB-8 at minus ends may localize a kinase that could phosphorylate dynein or its cargo. A potential candidate would be JNK, which is required for DCV capture and SVP clustering (Bharat et al., 2017; Wu et al., 2013). It would be interesting to test whether VAB-8 could facilitate interactions between JNK and dynein at synapses.

Methods

Strains and maintenance

All *C. elegans* strains were cultured on nematode growth medium plates seeded with *E. coli* OP50 as previously described (Brenner, 1974). Animals were grown at 20°C prior to experiments/injections and at room temperature afterward. The N2 Bristol strain was as wildtype for outcrosses. *C. elegans* strains used are listed in S1 Table.

Genetic screen

We performed a visual forward F2 genetic screen of ~ 2,000 haploid genomes. Ethyl methanesulfonate (EMS) was used to induced random germline mutations in animals carrying the *wyIs802 [Pitr-1::PTRN-1::YFP]* marker. Mutagenized worms were scored for changes in YFP::PTRN-1a in DA9. Homozygous mutants were rescued and outcrossed 5 times with N2 males prior to phenotypic analysis and whole-genome sequencing. Genomic DNA was purified with Phenol/$CHCl_3$ (Invitrogen-Thermo Fisher) and precipitated with ethanol/ $NaCH_3COO$ (Sigma-Aldrich). DNA was resuspended and solubilized in DNAse-free water (Sigma-Aldrich) and sequenced on Illumina Hi-Seq machines at the Yale Center for Genome Analysis. Sequencing data was analyzed by using tools on Galaxy Project. Briefly, reads were aligned against *C. elegans* N2 genome as a reference. Variants were called and filtered to isolate strain-specific single-nucleotide and indel mutations. The causality of mutations in *vab-8* and *plr-1* for the phenotypes was confirmed by rescue experiments, testing additional alleles and generation of additional mutants using CRISPR.

Cloning and constructs

All plasmids were generated by Gibson Assembly and confirmed by Sanger sequencing. cDNA was prepared from *C.elegans* lysates according to standard procedures. Sequences and plasmids are freely available upon request.

CRISPR/Cas9 genome editing

We used CRISPR to generate *shy72* and *shy73* mutations in *vab-8* near the *shy8* mutation in order to confirm the causality of mutations in that region to the *Vab-8* phenotype and in order to produce double mutants *vab-8, nrx-1* since the two genes are too close to each other for generating recombinants. We followed the protocol of (Dokshin et al., 2018). Cas9 protein was purchased from IDT. sgRNA was synthesized using EnGen kit from NEB using the following primer: ttctaatacgactcactatagTCAATCCCTCCCATGCTCCGgttttagagctaga. The following single strand repair template was used to induce STOP mutations: AACACACAACTGCCACGACGGTTGTATTCATTCAATCCCTCCCATGCTATAAGGATCCCTAATTAACCGTAGACACA CGCCATTCCTCTCTGCATCACTGAAACTGTACGACGA. Sanger sequencing was used to confirm the repair.

Fluorescence microscopy

Animals were synchronized as L4 larvae and grown for an additional 20-24 hrs at 20 degrees to reach adulthood. We immobilized worms on agar pads with 5-10 mM Levamisole in M9 buffer for standard fluorescence imaging. Images were acquired through an HC PL APO 63x/1.40NA OIL CS2 objective or a PL APO 40x/1.30NA CS2 objective built on a Laser Safe DMi8 inverted microscope (Leica) equipped with a VT-iSIM system (BioVision). Images were captured with an ORCA-Flash4.0 camera

(Hamamatsu) and controlled by MetaMorph Advanced Confocal Acquisition Software Package. For any given set of data, the same settings (laser power, exposure time, and gain) were used.

For time-lapse imaging, animals were incubated in levamisole (0.5 mM) in M9 at room temperature for 5 min prior to mounting on 10% agarose slide in M9 without paralytics, ensuring a low concentration of levamisole that was determined not to produce artifacts. Movies were collected on an Olympus BX61 microscope equipped with a Hamamatsu ORCA-Flash4.0 LT camera at 3 or 10 Hz (microtubules and synaptic vesicles respectively) for 3 min. Image acquisition was monitored by Volocity 2.0 (Quorum technologies). For any given set of data, the same settings (laser power, exposure time, and gain) were used. FRAP of GFP::RAB-3 and VAB-8::GFP was achieved by a 50 milliseconds pulse of 488-laser with a Perkin-Elmer Photokinesis unit.

Fluorescence quantification

Raw data were exported for analysis on ImageJ or MATLAB. Kymographs were generated using the ImageJ KymoResliceWide plugin following correction for animal movement using the StackReg plugin. Traces on kymographs were analyzed manually and data was exported to Excel and Igor Pro 8 for further analysis. To quantify the number of synapses, a line-scanning method along the axon was used to obtain the GFP::CLA-1 fluorescent profile. We used the same criterion as (Kurshan et al., 2018) to count a peak in the signal as a synapse (>5% of the maximum) for consistency with previous literature. Note that this criterion usually leads to the scoring of the fainter CLA-1 puncta in *nrx-1* mutants (highlighted Figure 1) as synapses. VAB-8::GFP axonal localization was resolved by drawing a region of interest (ROI) around the axon. Based on the intensity histogram, a default threshold was applied to the ROI to create a binary mask. The mask was firstly treated with the built-in Watershed segmentation algorithm to better define nearby puncta. Lastly, the number of puncta and their intensity were assessed by using the Analyze Particle function provided in ImageJ. PTRN-1 puncta spacing was quantified by measuring the distance between neighboring YFP::PTRN-1a puncta in the axonal region of interest. A custom MATLAB code (available upon request) was used to analyze the distribution of GFP::TBA-1 around RFP::PTRN-1 peaks. Briefly, the code determines the location of PTRN-1 peaks and averages GFP::TBA-1 in a 15-pixel region around each peak. As a control, the midway point between two peaks is used. To average the signal across multiple animals, the “on peak” traces were normalized by “off peak traces” in order to prevent variability in marker expression to impact the analysis. Axonal microtubule organization and minus-end analysis was done using a previously described and validated MATLAB code (Yogev et al., 2016), which is available upon request.

Single-molecule motility assays

To generate pMT-VAB-8-mNeonGreen plasmid, VAB-8 was amplified by PCR from P*mig13*::*vab-8* and subcloned into pMT-mNeonGreen vector.

Drosophila S2 cells were cultured in Schneider’s *Drosophila* medium (Gibco) supplemented with 10% (vol/vol) FBS (HyClone) at 26°C. Plasmid for expression of VAB-8-mNeonGreen in the pMT vector was transfected into S2 cells using CellfecinII (Invitrogen) according to manufacturer’s instructions. Expression of VAB8-mNeonGreen was induced by adding 1mM $CuSO_4$ to the medium after 4-5h transfection. To prepare cell lysate for single molecule assays, S2 cells were harvested after 48h post-transfection. The cells were centrifuged at low-speed at 4°C. The cell pellet was washed with PBS buffer and resuspended in ice-cold lysis buffer (25 mM HEPES/KOH, 115 mM potassium acetate, 5 mM sodium

acetate, 5 mM MgCl2, 0.5 mM EGTA, and 1% Triton X-100, pH 7.4) freshly supplemented with 1 mM ATP, 1 mM PMSF, and protease inhibitors (Sigma-Aldrich). After the cell lysate was clarified by centrifugation at full-speed at 4°C, aliquots of the supernatant were snap frozen in liquid nitrogen and stored at -80°C until further use.

HiLyte647-labeled microtubules were polymerized from purified tubulin including 10% Hily647-labeled tubulin (Cytoskeleton) in BRB80 buffer (80 mM Pipes/KOH pH 6.8, 1 mM $MgCl_2$, and 1 mM EGTA) supplemented with 1 mM GTP and 2.5 mM $MgCl_2$ at 37°C for 30 min. 20 µM taxol in prewarmed BRB80 buffer was added and incubated at 37°C for additional 30 min to stabilize microtubules. Microtubules were stored in the dark at room temperature for further use. A flow cell (~10 µl volume) was assembled by attaching a clean #1.5 coverslip (Fisher Scientific) to a glass slide (Fisher Scientific) with two strips of double-sided tape. Polymerized microtubules were diluted in BRB80 buffer supplemented with 10 µM taxol and then were infused into flow cells and incubated for 5 min at room temperature for nonspecific adsorption to the coverslips. Subsequently, blocking buffer [1mg/ml casein and 10 µM taxol in P12 buffer] was infused and incubated for 5min. Finally, kinesin motors (0.5-2 µl cell lysate) in the motility mixture [2 mM ATP, 3 mg/ml casein, 10 µM taxol, and oxygen scavenging in P12 buffer] was added to the flow cells. The flow-cell was sealed with molten paraffin wax.

Images for single molecule assay were acquired by TIRF microscopy using an inverted microscope Ti-E/B (Nikon) equipped with the perfect focus system (Nikon), a 100× 1.49 NA oil immersion TIRF objective (Nikon), three 20-mW diode lasers (488 nm, 561 nm, and 640 nm) and an electron-multiplying charge-coupled device detector (iXon X3DU897; Andor Technology). Image acquisition was controlled using Nikon Elements software and all assay were performed at room temperature. Images were acquired continuously at 200 ms per frame for 40 s. Maximum-intensity projections were generated and the kymographs were produced by drawing along tracks of motors (width= 3 pixels) using ImageJ.

Statistical analysis

Statistical analysis was performed on Igor Pro 8, Prism 9 (GraphStats), and SPSS (IBM). Data were considered significant at $p \leq 0.050$ and are plotted as the means with SEM. Each data set was compared using a Mann–Whitney *U* test unless otherwise specified. A Student *t* test was used to compare data groups when both passed the normality test (Kolmogorov–Smirnov).

Strain list

Strain name	Genotype
TV18675	*wyIs685 [Pmig-13::cla-1::gfp, Pmig-13::rab-3::tdTomato, Podr-1::gfp]*
MTS473	*plr-1(shy20); wyIs685 [Pmig-13::cla-1::gfp, Pmig-13::rab-3::tdTomato, Podr-1::gfp]*
MTS942	*plr-1(shy20); wyIs685 [Pmig-13::cla-1::gfp, Pmig-13::rab-3::tdTomato, Podr-1::gfp]*; *shyEx241* [P*mig-13*::*plr-1*::*scarlet*, P*unc-122*::*rfp*]
MTS900	*plr-1(shy20); wyIs685 [Pmig-13::cla-1::gfp, Pmig-13::rab-3::tdTomato, Podr-1::gfp]; shyEx234 [Pmig-13::plr-1(Δ317-358::scarlet), Punc-122::rfp]*
MTS962	*nrx-1(wy778), wyIs685 [Pmig-13::cla-1::gfp, Pmig-13::rab-3::tdTomato, Podr-1::gfp]*
MTS735	*mig-1(e1787); wyIs685 [Pmig-13::cla-1::gfp, Pmig-13::rab-3::tdTomato, Podr-1::gfp]*
MTS716	*mig-1(e1787); plr-1(shy20); wyIs685 [Pmig-13::cla-1::gfp, Pmig-13::rab-3::tdTomato, Podr-1::gfp]*

MTS963	*mig-1(e1787); plr-1(shy20); wyIs685 [Pmig-13::cla-1::gfp, Pmig-13::rab-3::tdTomato, Podr-1::gfp]; shyEx249 [Pmig-13::mig-1, Podr-1::rfp]*
MTS964	*mig-1(e1787); nrx-1(wy778), wyIs685 [Pmig-13::cla-1::gfp, Pmig-13::rab-3::tdTomato, Podr-1::gfp]*
MTS561	*lin-17(n3091); plr-1(shy20); wyIs685 [Pmig-13::cla-1::gfp, Pmig-13::rab-3::tdTomato, Podr-1::gfp]*
MTS547	*lin-17(n3091); wyIs685 [Pmig-13::cla-1::gfp, Pmig-13::rab-3::tdTomato, Podr-1::gfp]*
MTS337	*wyEx677 [Pmig-13::lin-17::yfp + Pmig-13::mCherry::rab-3]*
MTS338	*plr-1(shy20); wyEx677 [Pmig-13::lin-17::yfp + Pmig-13::mCherry::rab-3]*
MTS234	*lin-17(n671); wyIs685 [Pmig-13::cla-1::gfp, Pmig-13::rab-3::tdTomato, Podr-1::gfp]*
MTS965	*plr-1(shy20); nrx-1(wy778), wyIs685 [Pmig-13::cla-1::gfp, Pmig-13::rab-3::tdTomato, Podr-1::gfp]*
MTS471	*vab-8(shy8), wyIs685 [Pmig-13::cla-1::gfp, Pmig-13::rab-3::tdTomato, Podr-1::gfp]*
MTS529	*ptrn-1(js1286); vab-8(shy8), wyIs685 [Pmig-13::cla-1::gfp, Pmig-13::rab-3::tdTomato, Podr-1::gfp]*
MTS955	*vab-8(shy8), wyIs685 [Pmig-13::cla-1::gfp, Pmig-13::rab-3::tdTomato, Podr-1::gfp]; shyEx247 [Pmig-13::vab-8::scarlet, Punc-122::rfp]*
MTS966	*vab-8(shy8), wyIs685 [Pmig-13::cla-1::gfp, Pmig-13::rab-3::tdTomato, Podr-1::gfp]; shyEx250 [Pmig-13::vab-8(Δ1-326)::scarlet, Podr-1::rfp]*
MTS920	*vab-8(shy8), wyIs685 [Pmig-13::cla-1::gfp, Pmig-13::rab-3::tdTomato, Podr-1::gfp]; shyEx235 [Pmig-13::vab-8(Δ713-1066)::scarlet, Podr-1::rfp]*
MTS923	*vab-8(shy8), wyIs685 [Pmig-13::cla-1::gfp, Pmig-13::rab-3::tdTomato, Podr-1::gfp]; shyEx236 [Pmig-13::vab-8(R278A)::scarlet, Podr-1::rfp]*
MTS976	*lin-44(n1792); wyIs685 [Pmig-13::cla-1::gfp, Pmig-13::rab-3::tdTomato, Podr-1::gfp]*
MTS977	*lin-44(n1792); vab-8(shy8), wyIs685 [Pmig-13::cla-1::gfp, Pmig-13::rab-3::tdTomato, Podr-1::gfp]*
MTS662	*lin-17(n3091); vab-8(shy8), wyIs685 [Pmig-13::cla-1::gfp, Pmig-13::rab-3::tdTomato, Podr-1::gfp]*
MTS925	*plr-1(shy20); vab-8(shy8), wyIs685 [Pmig-13::cla-1::gfp, Pmig-13::rab-3::tdTomato, Podr-1::gfp]*
MTS335	*vab-8(shy8); wyEx677 [Pmig-13::lin-17::yfp + Pmig-13::mCherry::rab-3]*
MTS729	*mig-1(e1787); vab-8(shy8), wyIs685 [Pmig-13::cla-1::gfp, Pmig-13::rab-3::tdTomato, Podr-1::gfp]*
MTS956	*vab-8(shy72), wyIs685 [Pmig-13::cla-1::gfp, Pmig-13::rab-3::tdTomato, Podr-1::gfp]*
MTS957	*vab-8(shy73), nrx-1(wy778), wyIs685 [Pmig-13::cla-1::gfp, Pmig-13::rab-3::tdTomato, Podr-1::gfp]*
MTS958	*nrx-1(wy778), wyIs685 [Pmig-13::cla-1::gfp, Pmig-13::rab-3::tdTomato, Podr-1::gfp]; shyEx248 [Pmig-13::vab-8, Punc-122::rfp]*
MTS538	*shyEx121 [Pitr-1::vab-8::gfp, Pmig-13::tagrfp, Pttx-3::rfp]*
MTS658	*shyEx175 [Pitr-1::vab-8::gfp, Pmig-13::rfp::ptrn-1a, Punc-122::rfp]*
MTS967	*noca-1(ok3692); shyEx121 [Pitr-1::vab-8::gfp, Pmig-13::tagrfp, Pttx-3::rfp]*
MTS546	*plr-1(shy20); shyEx121 [Pitr-1::vab-8::gfp, Pmig-13::tagrfp, Pttx-3::rfp]*
MTS736	*mig-1(e1787); plr-1(shy20); shyEx121 [Pitr-1::vab-8::gfp, Pmig-13::tagrfp, Pttx-3::rfp]*
MTS968	*nrx-1(wy778); shyEx121 [Pitr-1::vab-8::gfp, Pmig-13::tagrfp, Pttx-3::rfp]*
MTS969	*mig-1(e1787); nrx-1(wy778); shyEx121 [Pitr-1::vab-8::gfp, Pmig-13::tagrfp, Pttx-3::rfp]*
MTS970	*plr-1(shy20); nrx-1(wy778); shyEx121 [Pitr-1::vab-8::gfp, Pmig-13::tagrfp, Pttx-3::rfp]*

MTS226	*tba-1(ok1135); wySi265 [Punc-4c::CRE; Punc-122::rfp]; wyIs463 [Pmig-13::STOP::gfp::tba-1; Podr-1::rfp]*
MTS516	*tba-1(ok1135); vab-8(shy8); wySi265 [Punc-4c::CRE; Punc-122::rfp]; wyIs463 [Pmig-13::STOP::gfp::tba-1; Podr-1::rfp]*
MTS427	*tba-1(ok1135); plr-1(shy20); wySi265 [Punc-4c::CRE; Punc-122::rfp]; wyIs463 [Pmig-13::STOP::gfp::tba-1; Podr-1::rfp]*
TV21554	*wyIs802 [Pitr-1::yfp::ptrn-1a, Podr-1::gfp]*
MTS126	*vab-8(shy8); wyIs802 [Pitr-1::yfp::ptrn-1a, Podr-1::gfp]*
MTS998	*nrx-1(wy778); wyIs802 [Pitr-1::yfp::ptrn-1a, Podr-1::gfp]*
MTS717	*mig-1(e1787); vab-8(shy8); wyIs802 [Pitr-1::yfp::ptrn-1a, Podr-1::gfp]*
MTS310	*vab-8(ev411); wyIs802 [Pitr-1::yfp::ptrn-1a, Podr-1::gfp]*
MTS284	*vab-8(e1017); wyIs802 [Pitr-1::yfp::ptrn-1a, Podr-1::gfp]*
MTS431	*plr-1(shy20); vab-8(shy8); wyIs802 [Pitr-1::yfp::ptrn-1a, Podr-1::gfp]*
MTS285	*vab-8(gm84); wyIs802 [Pitr-1::yfp::ptrn-1a, Podr-1::gfp]*
MTS465	*unc-104(e1265); vab-8(shy8); wyIs803 [Pitr-1::yfp::ptrn-1a, Podr-1::gfp]*
MTS534	*tbb-2(qt1); vab-8(shy8); wyIs802 [Pitr-1::yfp::ptrn-1a, Podr-1::gfp]*
MTS979	*tbb-2(qt1); vab-8(shy8); wyIs685 [Pmig-13::cla-1::gfp, Pmig-13::rab-3::tdTomato, Podr-1::gfp]*
MTS978	*unc-104(e1265); wyIs803 [Pitr-1::yfp::ptrn-1a, Podr-1::gfp]*
MTS980	*tbb-2(qt1); wyIs685 [Pmig-13::cla-1::gfp, Pmig-13::rab-3::tdTomato, Podr-1::gfp]*
MTS981	*tbb-2(qt1); wyIs802 [Pitr-1::yfp::ptrn-1a, Podr-1::gfp]*
MTS226	*tba-1(ok1135); wySi265 [Punc-4c::CRE; Punc-122::rfp]; wyIs463 [Pmig-13::STOP::gfp::tba-1; Podr-1::rfp]; wyEx7468 [Pmig-13::STOP::tagrfp; Podr-1::gfp]*
MTS613	*tba-1(ok1135); vab-8(shy8); wySi265 [Punc-4c::CRE; Punc-122::rfp]; wyIs463 [Pmig-13::STOP::gfp::tba-1; Podr-1::rfp]; wyEx7468 [Pmig-13::STOP::tagrfp; Podr-1::gfp]*
MTS428	*tba-1(ok1135); plr-1(shy20); wySi265 [Punc-4c::CRE; Punc-122::rfp]; wyIs463 [Pmig-13::STOP::gfp::tba-1; Podr-1::rfp]; wyEx7468 [Pmig-13::STOP::tagrfp; Podr-1::gfp]*
MTS482	*vab-8(shy8); wyIs802 [Pitr-1::yfp::ptrn-1a, Podr-1::gfp]; shyEx247 [Pmig-13::vab-8::scarlet, Punc-122::rfp]*
MTS479	*vab-8(shy8); wyIs802 [Pitr-1::yfp::ptrn-1a, Podr-1::gfp]; shyEx250 [Pmig-13::vab-8(Δ1-326)::scarlet, Podr-1::rfp]*
MTS990	*vab-8(shy8); wyIs802 [Pitr-1::yfp::ptrn-1a, Podr-1::gfp]; shyEx235 [Pmig-13::vab-8(Δ713-1066)::scarlet, Podr-1::rfp]*
MTS991	*vab-8(shy8); wyIs802 [Pitr-1::yfp::ptrn-1a, Podr-1::gfp]; shyEx236 [Pmig-13::vab-8(R278A)::scarlet, Podr-1::rfp]*
MTS92	*plr-1(shy20); wyIs802 [Pitr-1::yfp::ptrn-1a, Podr-1::gfp]*
MTS340	*plr-1(hd129); wyIs802 [Pitr-1::yfp::ptrn-1a, Podr-1::gfp]*
MTS637	*mig-1(e1787); plr-1(shy20); wyIs802 [Pitr-1::yfp::ptrn-1a, Podr-1::gfp]*
MTS992	*plr-1(shy20); wyIs802 [Pitr-1::yfp::ptrn-1a, Podr-1::gfp]; shyEx241 [Pmig-13::plr-1::scarlet, Punc-122::rfp]*
MTS993	*plr-1(shy20); wyIs802 [Pitr-1::yfp::ptrn-1a, Podr-1::gfp]; shyEx234 [Pmig-13::plr-1(Δ317-358::scarlet), Punc-122::rfp]*
MTS510	*wyIs802 [Pitr-1::yfp::ptrn-1a, Podr-1::gfp], wySi265 [Punc-4c::CRE; Punc-122::rfp]; wyIs363 [Pmig-13::STOP::tdTomato::rab-3; Podr-1::gfp]*
MTS609	*wyIs802 [Pitr-1::yfp::ptrn-1a, Podr-1::gfp], wySi265 [Punc-4c::CRE; Punc-122::rfp]; vab-8(shy8); wyIs363 [Pmig-13::STOP::tdTomato::rab-3; Podr-1::gfp]*

MTS661	*wyIs802 [Pitr-1::yfp::ptrn-1a, Podr-1::gfp], wySi265 [Punc-4c::CRE; Punc-122::rfp]; plr-1(shy20); wyIs363 [Pmig-13::STOP::tdTomato::rab-3; Podr-1::gfp]*
MTS994	*shyEx251[Pitr-1::noca-1b::gfp, Podr-1::rfp]*
MTS995	*vab-8(shy8); shyEx251[Pitr-1::noca-1b::gfp, Podr-1::rfp]*
MTS996	*plr-1(shy20); shyEx251[Pitr-1::noca-1b::gfp, Podr-1::rfp]*
TV9315	*wyIs251 [Pmig-13::pB::gfp::rab-3, Podr-1::gfp]*
MTS535	*vab-8(shy8); wyIs251 [Pmig-13::rab-3::gfp, Podr-1::gfp]*
MTS463	*plr-1(shy20); wyIs251 [Pmig-13::pB::gfp::rab-3, Podr-1::gfp]*
MTS774	*dhc-I(js319); vab-8(shy8), wyIs685 [Pmig-13::cla-1::gfp, Pmig-13::rab-3::tdTomato, Podr-1::gfp]*
MTS773	*nud-2(ok949); vab-8(shy8), wyIs685 [Pmig-13::cla-1::gfp, Pmig-13::rab-3::tdTomato, Podr-1::gfp]*
MTS986	*unc-104(wy711); vab-8(shy8), wyIs685 [Pmig-13::cla-1::gfp, Pmig-13::rab-3::tdTomato, Podr-1::gfp]*
MTS987	*arl-8(tm2388); vab-8(shy8), wyIs685 [Pmig-13::cla-1::gfp, Pmig-13::rab-3::tdTomato, Podr-1::gfp]*
MTS983	*dhc-I(js319); wyIs685 [Pmig-13::cla-1::gfp, Pmig-13::rab-3::tdTomato, Podr-1::gfp]*
MTS982	*nud-2(ok949); wyIs685 [Pmig-13::cla-1::gfp, Pmig-13::rab-3::tdTomato, Podr-1::gfp]*
MTS988	*unc-104(wy711); wyIs685 [Pmig-13::cla-1::gfp, Pmig-13::rab-3::tdTomato, Podr-1::gfp]*
MTS989	*arl-8(tm2388); wyIs685 [Pmig-13::cla-1::gfp, Pmig-13::rab-3::tdTomato, Podr-1::gfp]*
MTS985	*dhc-I(js319); plr-1(shy20); wyIs685 [Pmig-13::cla-1::gfp, Pmig-13::rab-3::tdTomato, Podr-1::gfp]*
MTS984	*dhc-I(js319); nrx-1(wy778); wyIs685 [Pmig-13::cla-1::gfp, Pmig-13::rab-3::tdTomato, Podr-1::gfp]*

Table S1: Description of alleles used

Allele	Molecular change	Effect on protein/function
vab-8(shy8)	Deletion and frameshift: 463KLYDELC to 463TDDKKR-Opal	Truncation of the protein before coiled-coil domain (CCD) (see Figure 2F) / null allele (see Figure S5)
vab-8(shy72)	CRISPR insertion R452Ochre	Truncation of the protein before CCD (see Figure 2F and Methods)
vab-8(ev411)	Substitution - Splice donor (G904A)	Truncation of the protein in motor domain (MD)
vab-8(e1017)	Substitution - Stop codon (R554OpaI)	Truncation of the protein in CCD
vab-8(gm84)	Substitution - Splice donor (G10,698A)	Truncation of the protein in CCD
plr-1(shy20)	Substitution - Stop codon (R188OpaI)	Truncation of the protein before transmembrane domain (TMD) (see Figure 1C).
plr-1(hd129)	Deletion	Truncation of the protein before TMD
lin-17(n3091)	Substitution - Stop codon (Q55Ochre)	Early truncation (before TM domains)
lin-17(n671)	Substitution - Stop codon (Q449Ochre)	Truncation of the protein after 6th TMD
mig-1(e1787)	Q277Ochre (transcript A) or Q281Ochre (transcript B)	Truncation between 3rd and 4th TM domains

nrx-1(wy778)	Deletion	Deletion covering C terminus of α and γ nrx-1 isoforms (including transmembrane and intracellular domain)
lin-44(n1792)	Substitution - Stop codon (W100Amber)	Truncation of the protein in WNT-1 domain
dhc-I(js319)	Substitution - Splice acceptor intron 12 (Cter)	Weak allele based on viability and comparison to other alleles (Koushika et al., 2004, Yogev et al., 2017)
nud-2(ok949)	Deletion	Truncation of the globular domain and CCD. Does not severly affect SVP transport (Ou et al., 2010)
unc-104(wy711)	Substitution - G313E	Weak allele (Wu et al, 2013)
unc-104(e1265)	Substitution - D1497N	Disruption of PH domain, strong loss of function but not null.
arl-8(tm2388)	Deletion in 3'UTR	Weak allele (Wu et al., 2013)
tbb-2(qt1)	Substitution - E198K	Temperature sensitive, attenuates microtubule dynamics in DA9 (Yogev et al., 2017)
noca-1(ok3692)	Deletion	Removes ninein homology domain (NHD), homozygous sterile.
ptrn-1(js1286)	Substitution - Stop codon (Y241Amber)	Truncation of the protein in calponin-homology (CH) domain

Acknowledgments

The authors would like to thank the Caenorhabditis Genetic Center (CGC) for strains. We also thank Kang Shen for sharing strains and D. Miller for the Prab-3::spGFP$_{1-10}$ strain. We thank members of the Yogev and Hammarlund labs for discussions and technical assistance. This work was supported by NIH R01-NS114400 and R35-GM131744.

Author contributions

S.B.G and S.Y designed the project, carried out experiments in *C. elegans* and wrote the manuscript. L.S.: Matlab codes for image analysis. S.C and C.K: cloning and imaging. Y.Y and K.J.V: design, imaging and interpretation of *in vitro* experiments.

Figure S1

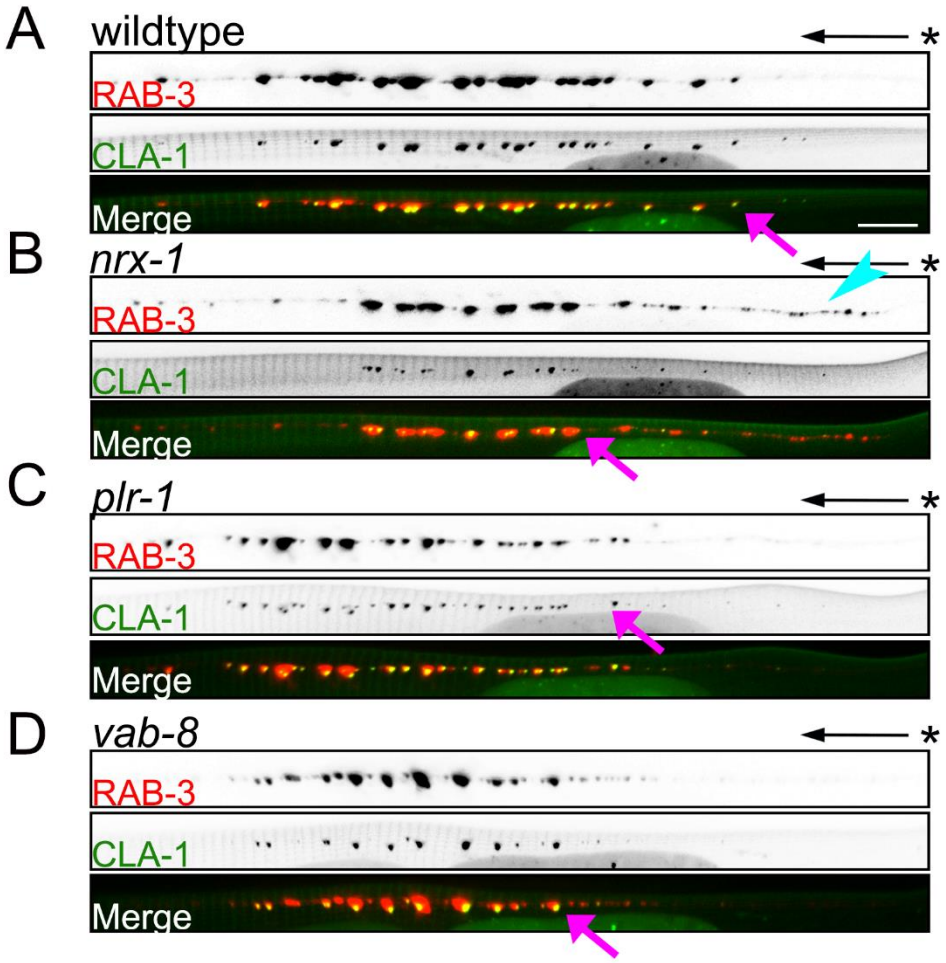

Figure S1: Normal synaptic vesicle clustering in *vab-8* and *plr-1* mutants

(A-D) *vab-8* and *plr-1* mutants phenocopy the missing proximal synapses of *nrx-1* but do not show vesicle clustering defects. Axons from wildtype (A), *nrx-1* (B), *plr-1* (C) and *vab-8* (D) expressing the active zone marker GFP::CLA-1 and the synaptic vesicle precursor marker tdTomato::RAB-3. * marks the turn of the commissure. Pink arrows point to the first synapse and arrowhead points to RAB-3 that is not associated with CLA in *nrx-1* mutants, indicating vesicle clustering defects. Scale bar = 5μm.

Figure S2

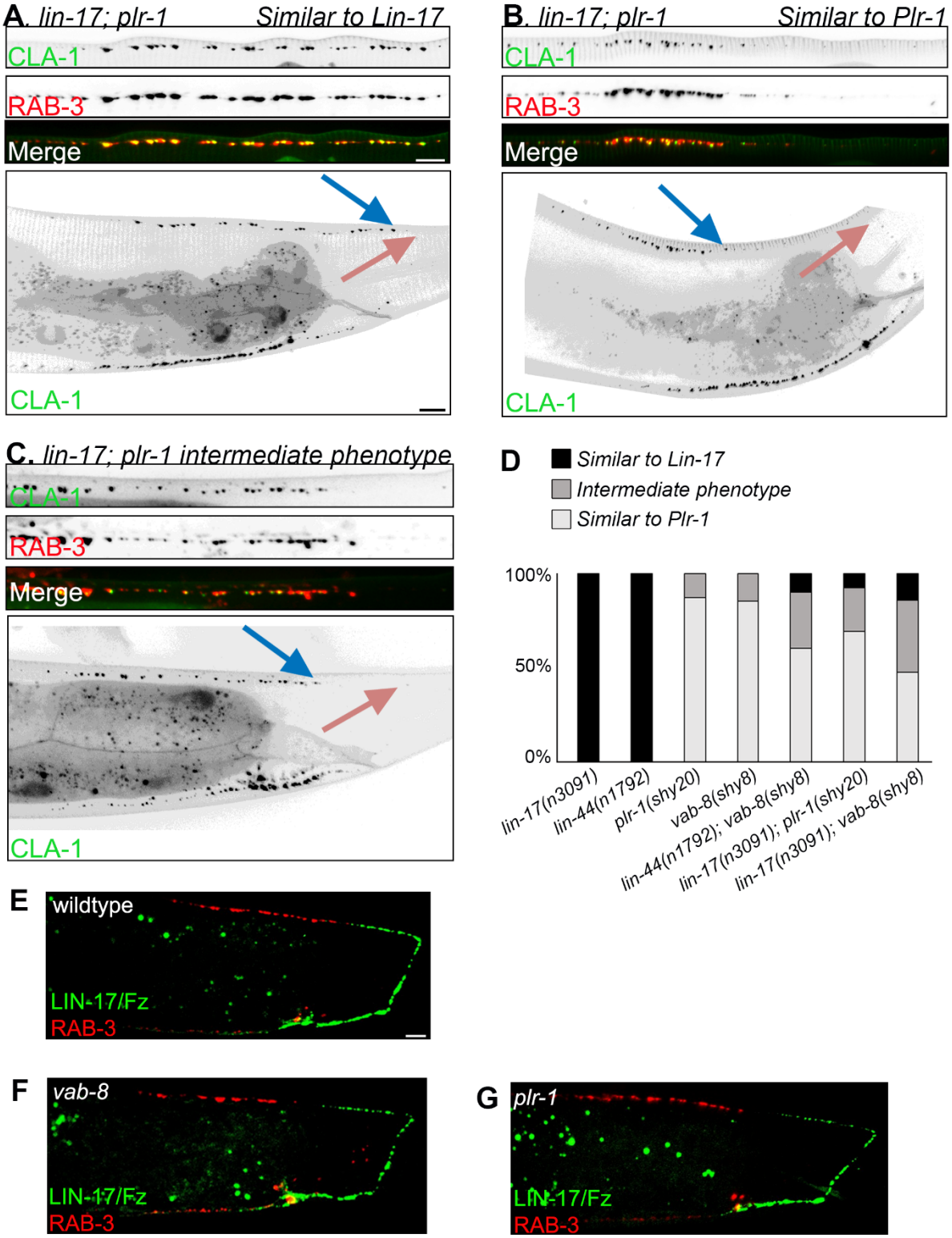
A. lin-17; plr-1
Similar to Lin-17
CLA-1
RAB-3
Merge
CLA-1
B. lin-17; plr-1
Similar to Plr-1
CLA-1
RAB-3
Merge
CLA-1
C. lin-17; plr-1 intermediate phenotype
CLA-1
RAB-3
Merge
CLA-1
D
Similar to Lin-17
Intermediate phenotype
Similar to Plr-1
100%
50%
0%
lin-17(n3091)
lin-44(n1792)
plr-1(shy20)
vab-8(shy8)
lin-44(n1792); vab-8(shy8)
lin-17(n3091); plr-1(shy20)
lin-17(n3091); vab-8(shy8)
E
wildtype
LIN-17/Fz
RAB-3
F
vab-8
LIN-17/Fz
RAB-3
G
plr-1
LIN-17/Fz
RAB-3

Figure S2: The Frizzled receptor LIN-17 does not act downstream of PLR-1

(A-C) Representative images of the different phenotypic classes used for quantifying genetic interactions. All images are from *lin-17; plr-1* double mutants expressing the active zone marker GFP::CLA-1 and the synaptic vesicle precursor marker tdTomato::RAB-3. Pink arrow marks the turn of the commissure and blue arrow marks the first synapse. "*Lin 17 phenotype"* is characterized by synapses starting immediately following the turn of the commissure or in the commissure itself. "*Plr-1 phenotype"* is defined as an asynaptic domain that is larger than in wildtype. "*intermediate phenotype"* is characterized by synapses starting at their normal location of closer to the turn of the commissure. **(D)** Quantification of the fraction of each phenotypic class in the indicated mutant backgrounds. **(E-G)** Representative images of wildtype (E), *vab-8* (F) and *plr-1* (G) adult worms expressing Frizzled/LIN-17::YFP and mCherry::RAB-3 in DA9. No apparent changes in the localization of Frizzled/LIN-17 is observed in the mutants. Scale bar = 5μm.

Figure S3

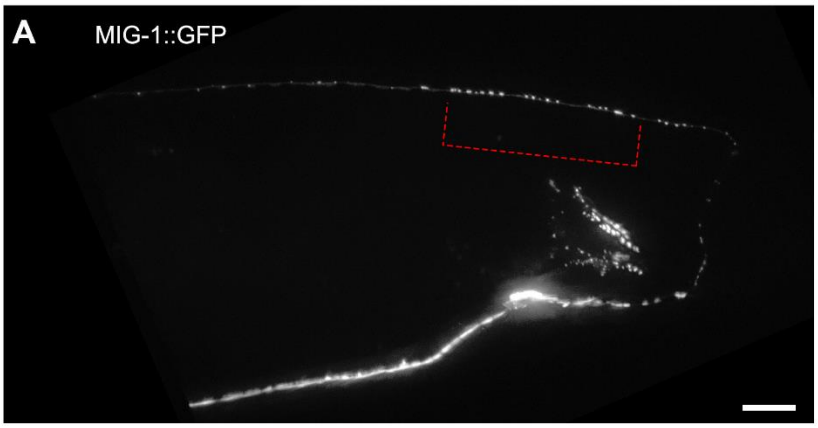

Figure S3: Axonal Frizzled/MIG-1 is localized to the region that shows synaptic defects in *plr1* mutants

Image shows adult worm expressing MIG-1::GFP in DA9. Red brackets indicate the location where synapses are missing in *plr-1* mutants. Scale bar = 5 μm.

Figure S4

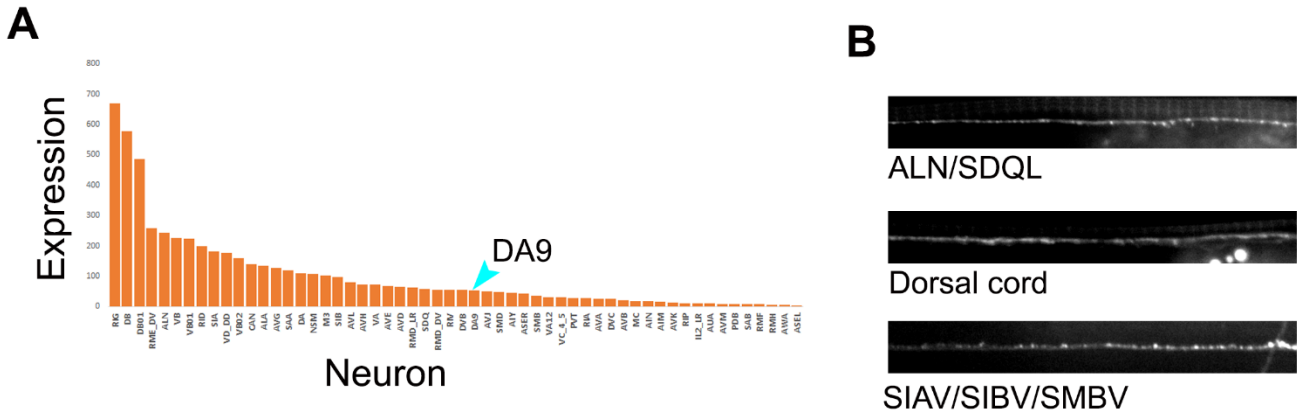

Figure S4: Endogenous VAB-8 expression and subcellular distribution

(A) Expression level of VAB-8 in single-cell RNAseq experiments from the CenGen project: https://cengen.shinyapps.io/CengenApp/. DA9 is indicated. **(B)** select examples of neurons where VAB-8 expression was sufficiently high to be detected with an endogenous 7X$spGFP_{11}$ tag and pan-neuronal expression of $spGFP_{1-10}$. Neuron identity was assigned based on the position of the axon (in most cases cell-bodies were too dim) and therefore contains some ambiguity.

Figure S5

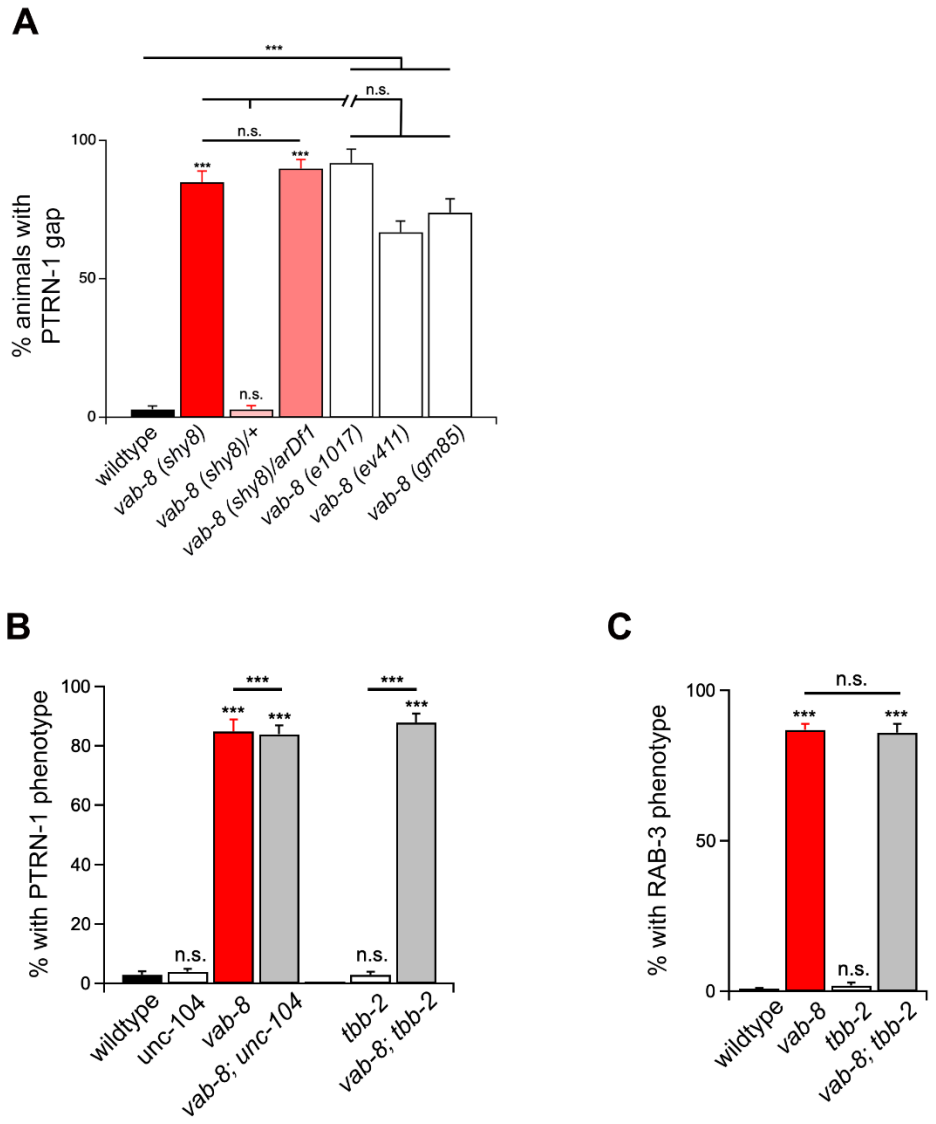

Figure S5: PTRN-1 gaps in *vab-8* mutants are not caused by the loss of synapses and loss of microtubule dynamicity does not lead to synapse elimination

(A) Comparison to previously characterized alleles and a deletion of the *vab-8* region shows that *shy8* is a genetic null allele. The presence of a PTRN-1::YFP "gap" around proximal synapses was scored. **(B)** The presence of PTRN-1 defects was tested in *unc-104(e1265)* in which DA9 synapses are largely eliminated and in *tbb-2(qt1)* mutants in which microtubule dynamicity is strongly suppressed in DA9. In both cases, no PTRN-1::YFP "gaps" are seen, and double mutants with *vab-8* do not modify the *Vab-8* phenotype, suggesting that loss of synapses and reduced microtubule dynamics do not drive the loss of PTRN-1::YFP in *vab-8* mutants. **(C)** Suppressing microtubule dynamics in *tbb-2(qt1)* mutants does not lead to loss of proximal synapses and does not modify the loss of proximal synapses in *vab-8* mutants. n = 100-150 per genotype, ***p<0.001; (Mann-Whitney U test).

Figure S6

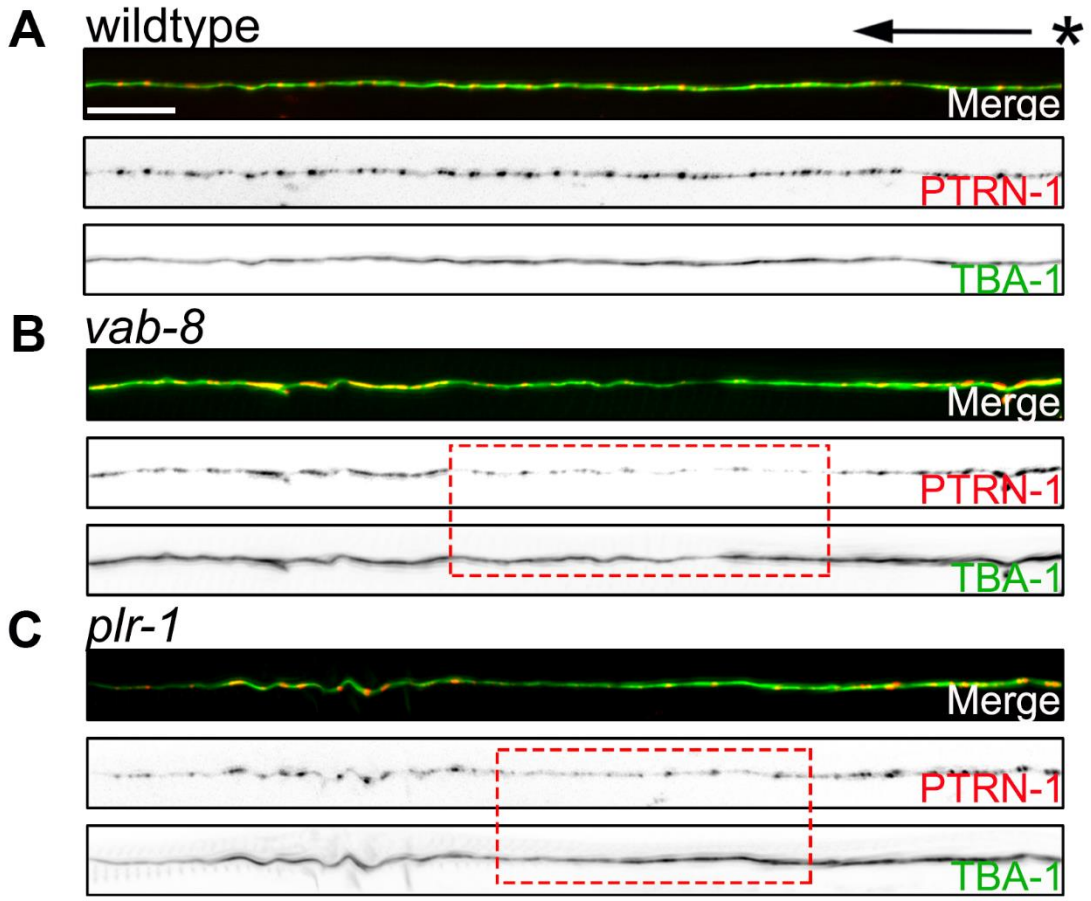

Figure S6: Microtubules are present in the region that shows PTRN-1 gaps in *vab-8* and *plr-1* mutants

(A-C) Images of axons from wildtype (A), *vab-8* (B) and *plr-1* (C) mutants expressing RFP::PTRN-1 and GFP::TBA-1/α-tubulin. Loss of PTRN-1 is not associated with loss of microtubules. * marks turn of the commissure. Dashed boxes highlight the affected region. Scale bar = 5μm.

Figure S6

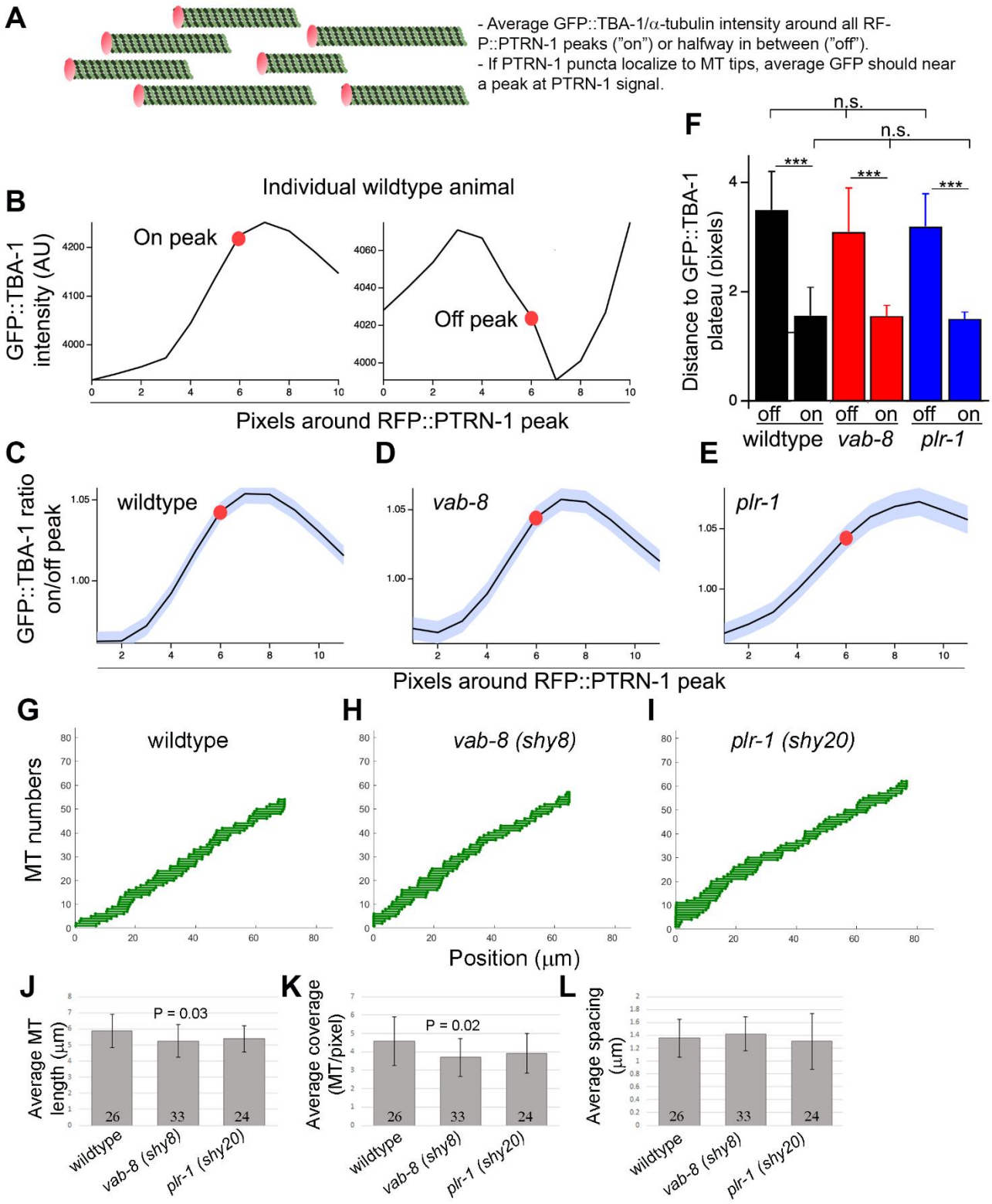
A
- Average GFP::TBA-1/α-tubulin intensity around all RF-P::PTRN-1 peaks ("on") or halfway in between ("off").
- If PTRN-1 puncta localize to MT tips, average GFP should near a peak at PTRN-1 signal.
B
Individual wildtype animal
GFP::TBA-1 intensity (AU)
On peak
Off peak
Pixels around RFP::PTRN-1 peak
F
n.s.
n.s.
***
Distance to GFP::TBA-1 plateau (pixels)
off on off on off on
wildtype vab-8 plr-1
C
D
E
GFP::TBA-1 ratio on/off peak
wildtype
vab-8
plr-1
Pixels around RFP::PTRN-1 peak
G
H
I
MT numbers
wildtype
vab-8 (shy8)
plr-1 (shy20)
Position (μm)
J
K
L
Average MT length (μm)
P = 0.03
Average coverage (MT/pixel)
P = 0.02
Average spacing (μm)
26
33
24
wildtype
vab-8 (shy8)
plr-1 (shy20)

Figure S7: Normal minus-end localization of PTRN-1 and normal microtubule organization in *plr-1* and *vab-8* mutants.

(A) Schematic of the concept for determining association of RFP::PTRN-1 with microtubule ends. The intensity of GFP::TBA-1 from an individual microtubule that harbors a given RFP::PTRN-1 punctum cannot be distinguished from that of other microtubules near it and so it is not possible to test where individual PTRN-1 puncta are localized along a given polymer. However, the average GFP::TBA-1 around many RFP::PTRN-1 puncta should increase and near a plateau is the puncta are associated with microtubule ends. **(B)** Example from a single wildtype animal: average GFP::TBA-1/α-tubulin around all RFP::PTRN-1 puncta from a 45 μm region around proximal synapses shows the expected increase. As a negative control, GFP::TBA-1/α-tubulin shows a decrease around the halfway point between PTRN-1 puncta. **(C-E)** Identical behavior of GFP::TBA-1/α-tubulin around RFP::PTRN-1 peaks in wildtype (C), *vab-8* (D) and *plr-1* (E) confirms that the faint RFP::PTRN-1 puncta in the mutants are associated with microtubule minus-ends. **(F)** Quantification of the distance between PTRN-1 puncta ("on") and the halfway between them ("off") to the nearest peak in GFP::TBA-1/α-tubulin intensity shows no difference between wildtype and mutants. **(G-L)** wildtype animals (G, J), *vab-8* mutants (H,K) and *plr-1* mutants (I,L) show overall similar microtubule organization. Microtubule organization parameters were determined as described in (Yogev et al., 2016). (G,H,I) show models for individual animals. (J) Average polymer length. (K) Average number of polymers per "cross section" of the axon at a given pixel. (L) Spacing between microtubule ends. n = 20-25.

References

Ahmari, S.E., Buchanan, J., and Smith, S.J. (2000). Assembly of presynaptic active zones from cytoplasmic transport packets. Nat Neurosci *3*, 445–451.

Akhmanova, A., and Steinmetz, M.O. (2019). Microtubule minus-end regulation at a glance. J Cell Sci *132*.

Bharat, V., Siebrecht, M., Burk, K., Ahmed, S., Reissner, C., Kohansal-Nodehi, M., Steubler, V., Zweckstetter, M., Ting, J.T., and Dean, C. (2017). Capture of Dense Core Vesicles at Synapses by JNK-Dependent Phosphorylation of Synaptotagmin-4. Cell Rep *21*, 2118–2133.

Biederer, T., and Südhof, T.C. (2000). Mints as adaptors. Direct binding to neurexins and recruitment of munc18. J Biol Chem *275*, 39803–39806.

Biederer, T., and Sudhof, T.C. (2001). CASK and protein 4.1 support F-actin nucleation on neurexins. J Biol Chem *276*, 47869–47876.

Brenner, S. (1974). The genetics of Caenorhabditis elegans. Genetics *77*, 71–94.

Brouwer, M., Farzana, F., Koopmans, F., Chen, N., Brunner, J.W., Oldani, S., Li, K.W., van Weering, J.R., Smit, A.B., Toonen, R.F., et al. (2019). SALM1 controls synapse development by promoting F-actin/PIP2-dependent Neurexin clustering. EMBO J *38*, e101289.

Cai, D., McEwen, D.P., Martens, J.R., Meyhofer, E., and Verhey, K.J. (2009). Single molecule imaging reveals differences in microtubule track selection between Kinesin motors. PLoS Biology *7*, e1000216.

Cavolo, S.L., Bulgari, D., Deitcher, D.L., and Levitan, E.S. (2016). Activity Induces Fmr1-Sensitive Synaptic Capture of Anterograde Circulating Neuropeptide Vesicles. J Neurosci *36*, 11781–11787.

Chen, X., Shibata, A.C., Hendi, A., Kurashina, M., Fortes, E., Weilinger, N.L., MacVicar, B.A., Murakoshi, H., and Mizumoto, K. (2018). Rap2 and TNIK control Plexin-dependent tiled synaptic innervation in C. elegans. ELife *7*, e38801.

Dean, C., Scholl, F.G., Choih, J., DeMaria, S., Berger, J., Isacoff, E., and Scheiffele, P. (2003). Neurexin mediates the assembly of presynaptic terminals. Nat Neurosci *6*, 708–716.

Dokshin, G.A., Ghanta, K.S., Piscopo, K.M., and Mello, C.C. (2018). Robust Genome Editing with Short Single-Stranded and Long, Partially Single-Stranded DNA Donors in Caenorhabditis elegans. Genetics *210*, 781–787.

Feng, C., Thyagarajan, P., Shorey, M., Seebold, D.Y., Weiner, A.T., Albertson, R.M., Rao, K.S., Sagasti, A., Goetschius, D.J., and Rolls, M.M. (2019). Patronin-mediated minus end growth is required for dendritic microtubule polarity. J Cell Biol *218*, 2309–2328.

Goodwin, S.S., and Vale, R.D. (2010). Patronin regulates the microtubule network by protecting microtubule minus ends. Cell *143*, 263–274.

Guedes-Dias, P., and Holzbaur, E.L.F. (2019). Axonal transport: Driving synaptic function. Science *366*.

Guedes-Dias, P., Nirschl, J.J., Abreu, N., Tokito, M.K., Janke, C., Magiera, M.M., and Holzbaur, E.L.F. (2018). Kinesin-3 Responds to Local Microtubule Dynamics to Target Synaptic Cargo Delivery to the Presynapse. Curr. Biol.

Guillabert-Gourgues, A., Jaspard-Vinassa, B., Bats, M.-L., Sewduth, R.N., Franzl, N., Peghaire, C., Jeanningros, S., Moreau, C., Roux, E., Larrieu-Lahargue, F., et al. (2016). Kif26b controls endothelial cell polarity through the Dishevelled/Daam1-dependent planar cell polarity-signaling pathway. Mol. Biol. Cell *27*, 941–953.

Hall, D.H., and Hedgecock, E.M. (1991). Kinesin-related gene unc-104 is required for axonal transport of synaptic vesicles in C. elegans. Cell *65*, 837–847.

Hao, H.-X., Xie, Y., Zhang, Y., Charlat, O., Oster, E., Avello, M., Lei, H., Mickanin, C., Liu, D., Ruffner, H., et al. (2012). ZNRF3 promotes Wnt receptor turnover in an R-spondin-sensitive manner. Nature *485*, 195–200.

Harada, A., Oguchi, K., Okabe, S., Kuno, J., Terada, S., Ohshima, T., Sato-Yoshitake, R., Takei, Y., Noda, T., and Hirokawa, N. (1994). Altered microtubule organization in small-calibre axons of mice lacking tau protein. Nature *369*, 488–491.

Hata, Y., Butz, S., and Südhof, T.C. (1996). CASK: a novel dlg/PSD95 homolog with an N-terminal calmodulin-dependent protein kinase domain identified by interaction with neurexins. J Neurosci *16*, 2488–2494.

He Chun-Wei, Liao Chien-Po, and Pan Chun-Liang Wnt signalling in the development of axon, dendrites and synapses. Open Biology *8*, 180116.

Jiang, K., Hua, S., Mohan, R., Grigoriev, I., Yau, K.W., Liu, Q., Katrukha, E.A., Altelaar, A.F.M., Heck, A.J.R., Hoogenraad, C.C., et al. (2014). Microtubule minus-end stabilization by polymerization-driven CAMSAP deposition. Dev Cell *28*, 295–309.

Klassen, M.P., and Shen, K. (2007). Wnt signaling positions neuromuscular connectivity by inhibiting synapse formation in C. elegans. Cell *130*, 704–716.

Koles, K., and Budnik, V. (2012). Wnt signaling in neuromuscular junction development. Cold Spring Harb Perspect Biol *4*.

Koo, B.-K., Spit, M., Jordens, I., Low, T.Y., Stange, D.E., van de Wetering, M., van Es, J.H., Mohammed, S., Heck, A.J.R., Maurice, M.M., et al. (2012). Tumour suppressor RNF43 is a stem-cell E3 ligase that induces endocytosis of Wnt receptors. Nature *488*, 665–669.

Koushika, S.P., Schaefer, A.M., Vincent, R., Willis, J.H., Bowerman, B., and Nonet, M.L. (2004). Mutations in Caenorhabditis elegans cytoplasmic dynein components reveal specificity of neuronal retrograde cargo. J Neurosci *24*, 3907–3916.

Kreutzberg, G.W. (1969). Neuronal dynamics and axonal flow. IV. Blockage of intra-axonal enzyme transport by colchicine. Proc. Natl. Acad. Sci. U.S.A. *62*, 722–728.

Kurshan, P.T., Merrill, S.A., Dong, Y., Ding, C., Hammarlund, M., Bai, J., Jorgensen, E.M., and Shen, K. (2018). γ-Neurexin and Frizzled Mediate Parallel Synapse Assembly Pathways Antagonized by Receptor Endocytosis. Neuron *100*, 150-166.e4.

Lüchtenborg, A.-M., Solis, G.P., Egger-Adam, D., Koval, A., Lin, C., Blanchard, M.G., Kellenberger, S., and Katanaev, V.L. (2014). Heterotrimeric Go protein links Wnt-Frizzled signaling with ankyrins to regulate the neuronal microtubule cytoskeleton. Development *141*, 3399–3409.

Maeder, C.I., Shen, K., and Hoogenraad, C.C. (2014). Axon and dendritic trafficking. Current Opinion in Neurobiology *27*, 165–170.

Marcette, J.D., Chen, J.J., and Nonet, M.L. (2014). The Caenorhabditis elegans microtubule minus-end binding homolog PTRN-1 stabilizes synapses and neurites. ELife *3*, e01637.

Meng, L., Chen, C., and Yan, D. (2016). Regulation of Gap Junction Dynamics by UNC-44/ankyrin and UNC-33/CRMP through VAB-8 in C. elegans Neurons. PLoS Genet *12*, e1005948.

Meng, W., Mushika, Y., Ichii, T., and Takeichi, M. (2008). Anchorage of microtubule minus ends to adherens junctions regulates epithelial cell-cell contacts. Cell *135*, 948–959.

Miech, C., Pauer, H.-U., He, X., and Schwarz, T.L. (2008). Presynaptic local signaling by a canonical wingless pathway regulates development of the Drosophila neuromuscular junction. J Neurosci *28*, 10875–10884.

Mizumoto, K., and Shen, K. (2013). Two Wnts instruct topographic synaptic innervation in C. elegans. Cell Reports *5*, 389–396.

Moffat, L.L., Robinson, R.E., Bakoulis, A., and Clark, S.G. (2014). The conserved transmembrane RING finger protein PLR-1 downregulates Wnt signaling by reducing Frizzled, Ror and Ryk cell-surface levels in C. elegans. Development *141*, 617–628.

Muhammad, K., Reddy-Alla, S., Driller, J.H., Schreiner, D., Rey, U., Böhme, M.A., Hollmann, C., Ramesh, N., Depner, H., Lützkendorf, J., et al. (2015). Presynaptic spinophilin tunes neurexin signalling to control active zone architecture and function. Nat Commun *6*, 8362.

Mukherjee, K., Sharma, M., Urlaub, H., Bourenkov, G.P., Jahn, R., Südhof, T.C., and Wahl, M.C. (2008). CASK Functions as a Mg2+-independent neurexin kinase. Cell *133*, 328–339.

Nibbeling, E.A.R., Duarri, A., Verschuuren-Bemelmans, C.C., Fokkens, M.R., Karjalainen, J.M., Smeets, C.J.L.M., de Boer-Bergsma, J.J., van der Vries, G., Dooijes, D., Bampi, G.B., et al. (2017). Exome sequencing and network analysis identifies shared mechanisms underlying spinocerebellar ataxia. Brain *140*, 2860–2878.

Niwa, S., Lipton, D.M., Morikawa, M., Zhao, C., Hirokawa, N., Lu, H., and Shen, K. (2016). Autoinhibition of a Neuronal Kinesin UNC-104/KIF1A Regulates the Size and Density of Synapses. Cell Reports *16*, 2129–2141.

Okada, Y., Yamazaki, H., Sekine-Aizawa, Y., and Hirokawa, N. (1995). The neuron-specific kinesin superfamily protein KIF1A is a unique monomeric motor for anterograde axonal transport of synaptic vesicle precursors. Cell *81*, 769–780.

Ou, C.Y., Poon, V.Y., Maeder, C.I., Watanabe, S., Lehrman, E.K., Fu, A.K., Park, M., Fu, W.Y., Jorgensen, E.M., Ip, N.Y., et al. (2010). Two cyclin-dependent kinase pathways are essential for polarized trafficking of presynaptic components. Cell *141*, 846–858.

Owald, D., Khorramshahi, O., Gupta, V.K., Banovic, D., Depner, H., Fouquet, W., Wichmann, C., Mertel, S., Eimer, S., Reynolds, E., et al. (2012). Cooperation of Syd-1 with Neurexin synchronizes pre- with postsynaptic assembly. Nat Neurosci *15*, 1219–1226.

Pack-Chung, E., Kurshan, P.T., Dickman, D.K., and Schwarz, T.L. (2007). A Drosophila kinesin required for synaptic bouton formation and synaptic vesicle transport. Nat. Neurosci. *10*, 980–989.

Pani, A.M., and Goldstein, B. (2018). Direct visualization of a native Wnt in vivo reveals that a long-range Wnt gradient forms by extracellular dispersal. Elife *7*.

Qu, X., Kumar, A., Blockus, H., Waites, C., and Bartolini, F. (2019). Activity-Dependent Nucleation of Dynamic Microtubules at Presynaptic Boutons Controls Neurotransmission. Curr Biol *29*, 4231-4240.e5.

Richardson, C.E., Spilker, K.A., Cueva, J.G., Perrino, J., Goodman, M.B., and Shen, K. (2014). PTRN-1, a microtubule minus end-binding CAMSAP homolog, promotes microtubule function in Caenorhabditis elegans neurons. ELife *3*, e01498.

Rizalar, F.S., Roosen, D.A., and Haucke, V. (2021). A Presynaptic Perspective on Transport and Assembly Mechanisms for Synapse Formation. Neuron *109*, 27–41.

Sanes, J.R., and Zipursky, S.L. (2020). Synaptic Specificity, Recognition Molecules, and Assembly of Neural Circuits. Cell *181*, 536–556.

Soundararajan, H.C., and Bullock, S.L. (2014). The influence of dynein processivity control, MAPs, and microtubule ends on directional movement of a localising mRNA. ELife *3*, e01596.

Stucchi, R., Plucińska, G., Hummel, J.J.A., Zahavi, E.E., Guerra San Juan, I., Klykov, O., Scheltema, R.A., Altelaar, A.F.M., and Hoogenraad, C.C. (2018). Regulation of KIF1A-Driven Dense Core Vesicle Transport: Ca2+/CaM Controls DCV Binding and Liprin-α/TANC2 Recruits DCVs to Postsynaptic Sites. Cell Rep *24*, 685–700.

Südhof, T.C. (2017). Synaptic Neurexin Complexes: A Molecular Code for the Logic of Neural Circuits. Cell *171*, 745–769.

Südhof, T.C. (2018). Towards an Understanding of Synapse Formation. Neuron *100*, 276–293.

Sugie, A., Hakeda-Suzuki, S., Suzuki, E., Silies, M., Shimozono, M., Möhl, C., Suzuki, T., and Tavosanis, G. (2015). Molecular Remodeling of the Presynaptic Active Zone of Drosophila Photoreceptors via Activity-Dependent Feedback. Neuron *86*, 711–725.

Susman, M.W., Karuna, E.P., Kunz, R.C., Gujral, T.S., Cantú, A.V., Choi, S.S., Jong, B.Y., Okada, K., Scales, M.K., Hum, J., et al. (2017). Kinesin superfamily protein Kif26b links Wnt5a-Ror signaling to the control of cell and tissue behaviors in vertebrates. Elife *6*.

Tan, R., Foster, P.J., Needleman, D.J., and McKenney, R.J. (2018). Cooperative Accumulation of Dynein-Dynactin at Microtubule Minus-Ends Drives Microtubule Network Reorganization. Dev Cell *44*, 233-247.e4.

Terabayashi, T., Sakaguchi, M., Shinmyozu, K., Ohshima, T., Johjima, A., Ogura, T., Miki, H., and Nishinakamura, R. (2012). Phosphorylation of Kif26b promotes its polyubiquitination and subsequent proteasomal degradation during kidney development. PLoS ONE *7*, e39714.

Vukoja, A., Rey, U., Petzoldt, A.G., Ott, C., Vollweiter, D., Quentin, C., Puchkov, D., Reynolds, E., Lehmann, M., Hohensee, S., et al. (2018). Presynaptic Biogenesis Requires Axonal Transport of Lysosome-Related Vesicles. Neuron *99*, 1216-1232.e7.

Wang, L., Tanaka, Y., Wang, D., Morikawa, M., Zhou, R., Homma, N., Miyamoto, Y., and Hirokawa, N. (2018). The Atypical Kinesin KIF26A Facilitates Termination of Nociceptive Responses by Sequestering Focal Adhesion Kinase. Cell Rep *24*, 2894–2907.

Wang, S., Wu, D., Quintin, S., Green, R.A., Cheerambathur, D.K., Ochoa, S.D., Desai, A., and Oegema, K. (2015). NOCA-1 functions with gamma-tubulin and in parallel to Patronin to assemble non-centrosomal microtubule arrays in. ELife *4*.

White, J.G., Southgate, E., Thomson, J.N., and Brenner, S. (1986). The structure of the nervous system of the nematode Caenorhabditis elegans. Philosophical Transactions of the Royal Society of London. Series B, Biological Sciences *314*, 1–340.

Wightman, B., Clark, S.G., Taskar, A.M., Forrester, W.C., Maricq, A.V., Bargmann, C.I., and Garriga, G. (1996). The C. elegans gene vab-8 guides posteriorly directed axon outgrowth and cell migration. Development *122*, 671–682.

van de Willige, D., Hoogenraad, C.C., and Akhmanova, A. (2016). Microtubule plus-end tracking proteins in neuronal development. Cell Mol Life Sci *73*, 2053–2077.

Woehlke, G., Ruby, A.K., Hart, C.L., Ly, B., Hom-Booher, N., and Vale, R.D. (1997). Microtubule Interaction Site of the Kinesin Motor. Cell *90*, 207–216.

Wojcik, M.H., Okada, K., Prabhu, S.P., Nowakowski, D.W., Ramsey, K., Balak, C., Rangasamy, S., Brownstein, C.A., Schmitz-Abe, K., Cohen, J.S., et al. (2018). De novo variant in KIF26B is associated with pontocerebellar hypoplasia with infantile spinal muscular atrophy. American Journal of Medical Genetics Part A *176*, 2623–2629.

Wolf, F.W., Hung, M.S., Wightman, B., Way, J., and Garriga, G. (1998). vab-8 is a key regulator of posteriorly directed migrations in C. elegans and encodes a novel protein with kinesin motor similarity. Neuron *20*, 655–666.

Wong, M.Y., Zhou, C., Shakiryanova, D., Lloyd, T.E., Deitcher, D.L., and Levitan, E.S. (2012). Neuropeptide delivery to synapses by long-range vesicle circulation and sporadic capture. Cell *148*, 1029–1038.

Wu, Y.E., Huo, L., Maeder, C.I., Feng, W., and Shen, K. (2013). The balance between capture and dissociation of presynaptic proteins controls the spatial distribution of synapses. Neuron *78*, 994–1011.

Xuan, Z., Manning, L., Nelson, J., Richmond, J.E., Colón-Ramos, D.A., Shen, K., and Kurshan, P.T. (2017). Clarinet (CLA-1), a novel active zone protein required for synaptic vesicle clustering and release. Elife *6*.

Yogev, S., and Shen, K. (2014). Cellular and molecular mechanisms of synaptic specificity. Annu Rev Cell Dev Biol *30*, 417–437.

Yogev, S., Cooper, R., Fetter, R., Horowitz, M., and Shen, K. (2016). Microtubule Organization Determines Axonal Transport Dynamics. Neuron *92*, 449–460.

Yogev, S., Maeder, C.I., Cooper, R., Horowitz, M., Hendricks, A.G., and Shen, K. (2017). Local inhibition of microtubule dynamics by dynein is required for neuronal cargo distribution. Nature Communications *8*, 15063.

Zhai, R.G., Vardinon-Friedman, H., Cases-Langhoff, C., Becker, B., Gundelfinger, E.D., Ziv, N.E., and Garner, C.C. (2001). Assembling the presynaptic active zone: a characterization of an active one precursor vesicle. Neuron *29*, 131–143.

Zhou, R., Niwa, S., Homma, N., Takei, Y., and Hirokawa, N. (2009). KIF26A is an unconventional kinesin and regulates GDNF-Ret signaling in enteric neuronal development. Cell *139*, 802–813.